BRD2 upregulation as a pan-cancer adaptive resistance mechanism to BET inhibition

Suyakarn Archasappawat[1,2], Juliette Jacques[1], EunJung Lee[1], and Chang-il Hwang[1,2]

[1] Department of Microbiology and Molecular Genetics, College of Biological Sciences, University of California, Davis, Davis, CA, United States

[2] University of California Davis Comprehensive Cancer Center, Sacramento, CA, United States

Corresponding author: cihwang@ucdavis.edu

Abstract

Bromodomain and extraterminal motif (BET) inhibitors, such as JQ1, are promising cancer therapeutics that target epigenetic regulators, particularly BRD4. However, resistance to BET inhibitors (BETi) limits their clinical utility, necessitating a better understanding of adaptive mechanisms. We identified BRD2 upregulation as a conserved response to BET inhibition across multiple cancer types and hypothesized that BRD2 compensates for BRD4 loss, sustaining essential transcriptional programs upon treatment. Consistent with this, BRD2 knockdown sensitized cancer cells to BETi *in vitro*, and combining BRD2 depletion and JQ1 treatment significantly impaired tumor growth *in vivo*. At the chromatin level, BRD2 and BRD4 ChIP-seq analysis of pancreatic cancer cells showed consistent BRD4 loss from chromatin after JQ1 treatment, while BRD2 displacement differed by sensitivity. Resistant cells maintained higher BRD2 occupancy than sensitive cells, suggesting a link between BRD2 retention and drug response. Mechanistically, NFYA mediates BRD2 upregulation as NFYA depletion attenuated BRD2 upregulation upon BETi treatment. Collectively, our findings establish BRD2 as a critical mediator of pan-cancer adaptive resistance to BETi and identify NFYA as a novel transcriptional regulator of this process. Co-targeting BRD2 or its regulatory network offers a rational strategy to enhance the durability and efficacy of BET-based therapies.

Keywords

BET inhibitor, resistance, pan-cancer, BRD2, BRD4

Introduction

Cancer progression can be driven by epigenetic reprogramming, which has recently been recognized as a fundamental hallmark of cancer (1, 2). Epigenetic alterations enable cancer cells to activate oncogenic programs, silence tumor suppressors and adapt to microenvironmental stress, thereby promoting cancer progression and metastasis (3). Importantly, while conferring plasticity and survival, these changes render cancer cells dependent on aberrant epigenetic regulation to sustain the malignant phenotype—vulnerabilities that can be therapeutically exploited. Central to this process is the molecular machinery that regulates epigenetic states, coordinated by three major classes of proteins: writers, readers, and erasers. Writers deposit modifications such as DNA methylation or histone acetylation, erasers remove them, and readers interpret these marks to regulate downstream transcriptional activity. Together, these mechanisms dynamically shape transcriptional programs, often hijacked during carcinogenesis.

Among these regulators, the BET (bromodomain and extra-terminal domain) family has drawn significant attention as a group of critical epigenetic readers. This family comprises four members—BRD2, BRD3, BRD4, and the testis-specific BRDT—all sharing a key structural feature: two tandem N-terminal bromodomains that recognize and bind acetylated lysine residues on histones to anchor transcriptional machinery at active chromatin (4, 5). Of these, BRD4 is the most extensively studied and plays a critical role at enhancer and super-enhancers (SE), large regulatory clusters that drive the expression of key oncogenes, such as *MYC* (6). In addition to tethering to acetylated chromatin, BRD4 also recruits and scaffolds the Mediator complex and the P-TEFb kinase to release paused RNA polymerase II, thereby sustaining high-level transcription of target genes (7). Collectively, the actions of BRD4 support self-reinforcing transcriptional programs driven by inherently unstable oncogenic *MYC* transcripts (3). Because direct pharmacologic inhibition of MYC has proven difficult, BRD4 represents an attractive therapeutic vulnerability. Small-molecule BET inhibitors (BETi) such as JQ1 competitively bind to the

54 bromodomains—most potently of BRD4—displacing them from chromatin and dismantling SE-
55 driven transcription (8). This results in rapid *MYC* downregulation and potent antitumor effects in
56 preclinical models, with notable success in MYC-addicted hematologic malignancies and an
57 increasing exploration across diverse cancer types (9-11).

58 Despite these promising preclinical outcomes, clinical responses to BETi have been modest and
59 short-lived, with resistance posing as a major barrier for translation (12-14). To date, most
60 mechanistic insights into BETi resistance have come from models of acquired resistance following
61 prolonged drug exposure, in which cancer cells undergo extensive transcriptional and epigenetic
62 rewiring. Such models may not reflect the clinically relevant dynamics of adaptive resistance,
63 defined by early and reversible changes that enable cancer cells to tolerate BET inhibition. A
64 deeper understanding of the early adaptive responses to BET inhibition could reveal
65 vulnerabilities that precede the emergence of acquired resistance and guide the development of
66 more effective upfront or combination therapies.

67 In this study, we uncovered upregulation of BRD2—a BRD4 paralog—as an adaptive response
68 to BET inhibition across multiple cancer types. Functionally, BRD2 knockdown (KD) sensitizes
69 tumors to the BETi JQ1, enhancing therapeutic efficacy in both *in vitro* and *in vivo* models.
70 Mechanistically, this upregulation is driven, at least in part, by increased expression of the
71 transcription factor NFYA. Notably, our results indicate that the extent of the initial BETi response
72 could help predict the benefit of combining BRD2 KD with JQ1. While all BETi-treated cells benefit
73 from the combination, the most substantial enhancements are observed in initially resistant
74 populations. These findings provide a rationale for incorporating BRD2 targeting into combination
75 strategies to enhance BETi potency and prolong their clinical benefit across diverse cancers.

Materials and methods

Cell lines and cell culture conditions

A diverse panel of mouse and human cancer cell lines was used in this study. All cells were maintained at 37°C in a humidified incubator with 5% CO_2 under standard conditions appropriate for each cell type. The base culture media included Dulbecco's Modified Eagle Medium (DMEM; Corning, 10-013-CV), RPMI-1640 (Gibco, 11875119), Iscove's Modified Dulbecco's Medium (IMDM; Gibco, 12440053), McCoy's 5A Modified Medium (Gibco, 16600082), Eagle's Minimum Essential Medium (EMEM; ATCC, 30-2003), and Advanced DMEM/F-12 (Gibco, 12634028). Unless otherwise specified, culture media were supplemented with 10% fetal bovine serum (FBS; GenClone, 25-550H) and 1% penicillin-streptomycin (P/S; Gibco, 15140-122). Triple-negative breast cancer (TNBC) cell lines were additionally supplemented with 10 mM HEPES (Gibco, 15630080), 1 μg/ml hydrocortisone, and 5 μg/ml insulin (Sigma-Aldrich, I0516-5ML). Cell line information, including species, tumor type, tissue origin, specific culture conditions, and corresponding sources and catalog numbers, is listed in the Table S1.

Drug compounds and treatment conditions

All compounds were purchased from the suppliers listed in Table S2 and dissolved in dimethyl sulfoxide (DMSO; Sigma-Aldrich, 472301-500ML) prior to use as stock solutions. Unless otherwise specified, treatments were performed at final concentration of 1 μM for 24 hours in mouse samples and 10 μM for 24 hours in human samples. For control conditions, cells were treated with DMSO at the same final concentration used to dissolve drug compounds.

Cell viability assay

Mouse cancer cells and A549, U251, and U2OS cells were seeded at 1,500 cells/well, while all other human cancer cells were seeded at 3,000 cells/well in 50 μl of complete medium into 96-well plates. Twenty-four hours after cell plating, drugs were serially diluted in complete medium

100 and 50 µl of the diluted compounds was added to each well. Cells were incubated for an
101 additional 72 hours before media were carefully removed. To assess cell viability, 100 µl of
102 diluted AlamarBlue solution prepared by mixing 200 µl of resazurin (Fisher Scientific,
103 AC418900010) in 50 ml of 1× PBS was added to each well. Plates were incubated at 37°C with
104 5% CO_2 for 3–4 hours. Absorbance at 570 nm was measured using a plate reader (SpectraMax
105 iD5 plate reader, Molecular Devices). Relative cell viability was calculated by normalizing the
106 absorbance of drug-treated wells to DMSO-treated controls. Dose–response curves were
107 generated using nonlinear regression (curve fitting) in GraphPad Prism version 10.6.0 (796).

108 **Colony formation assay**

109 One thousand cells were seeded per well in 6-well plates. After 1–3 days, cells were treated with
110 JQ1 (50–100 nM) for 7–10 days, with fresh drug-containing medium replaced every 2–3 days. At
111 the endpoint, cells were fixed with 100% methanol (15 minutes, room temperature) and stained
112 with 0.1% (w/v) crystal violet (Spectrum chemical, TCI-C0428-100G) in 20% methanol. Plates
113 were rinsed under running tap water until excess stain was no longer visible, air-dried
114 completely, and scanned (HP LaserJet Pro). Colony area and staining intensity were quantified
115 in ImageJ using the ColonyArea plugin.

116 **shRNA construct generation via pLKO.1 cloning**

117 For the generation of shRNA constructs, the pLKO.1-puro vector (Addgene #8453) was used. A
118 total of 6 µg of plasmid DNA was digested with 1 µl EcoRI-HF (NEB, R3101T), 1 µl AgeI-HF
119 (NEB, R3552S), and 5 µl rCutSmart Buffer (NEB, B6004S) in a 50 µl reaction and incubated at
120 37°C for 3 hours. To prevent vector self-ligation, 1 µl Quick CIP (NEB, M0525S) was added and
121 incubated for an additional hour at 37°C. The digested vector was purified using the PureLink
122 PCR purification kit (Invitrogen, K310002). For oligonucleotide preparation, 1 µl of forward and
123 reverse primers (each at 100 µM) were combined with 1 µl 10× T4 DNA ligase buffer (NEB,

124 B0202S), 0.5 µl T4 Polynucleotide Kinase (NEB, M0201S), and 6.5 µl nuclease-free water. The
125 reaction was incubated at 37°C for 30 minutes, then heated to 95 °C for 5 minutes, followed by a
126 gradual ramp down to 25°C at 5 °C/minute for annealing. The annealed primers were diluted
127 1:200 before ligation. Ligation reactions were performed by mixing 50 ng of digested pLKO.1
128 vector, 1 µl diluted annealed oligos, 1 µl 10× T4 ligase buffer (NEB, B0202S), 1 µl T4 DNA ligase
129 (NEB, M0202S), and water to a final volume of 10 µl. The mixture was incubated at room
130 temperature for 30 minutes. For transformation, 3 µl of the ligation mix was added to 30 µl XL10-
131 Gold ultracompetent cells (Agilent, 50-125-094). After 5 minutes on ice, cells were heat-shocked
132 at 42°C for 90 seconds, returned to ice for another 5 minutes, and plated on LB agar (Fisher
133 Scientific, BP1427-500) supplemented with 1× ampicillin (RPI, C802G69) using 4.5 mm sterile
134 rattler plating beads (Zymo Research, S1001). Plates were incubated overnight at 37°C (~16
135 hours). At least 6 individual colonies were miniprepped using Zyppy Plasmid Miniprep Kit (Zymo
136 Research, D4019). Plasmid inserts were verified by Sanger sequencing (GENEWIZ) using
137 primers targeting the U6 promoter. Resulting sequences were aligned to reference in Benchling
138 to confirm correct oligo insertion. Information about the short hairpin RNA (shRNA) constructs
139 used in this study, including the target gene, sequence ID, and oligonucleotide sequences, is
140 summarized in the Table S3.

141 **Lentiviral production and transduction**

142 Lentiviral particles were produced by transfecting HEK293T cells using a standard third-
143 generation packaging system. Briefly, 5×10^6 HEK293T cells were seeded in 10 cm culture
144 dishes. After 18–24 hours, the medium was replaced with DMEM supplemented with 10% FBS
145 (without P/S). Cells were then transfected with 10 µg of transfer plasmid (e.g., shRNA
146 constructs), 8 µg of psPAX2 (Addgene #12260), and 2 µg of pMD2.G (Addgene #12259), using
147 X-tremeGENE 360 transfection reagent (Roche, 8724156001) at a 1:3 DNA-to-reagent ratio,
148 following the manufacturer's instructions. After 48–72 hours, the viral supernatant was collected,

149 centrifuged at 1,100 rpm for 5 minutes to remove cell debris, and filtered through a 0.45 μm PES
150 filter (Cytiva, 28143-312). The resulting virus-containing media were used to transduce target
151 cells in the presence of polybrene (MilliporeSigma, C788D57) at a final concentration of 1 μg/ml.
152 Twenty-four hours after transduction, cells were selected with 2 μg/ml puromycin (Thermo
153 Scientific, 53-79-2) for at least 72 hours. Successful gene knockdown was subsequently
154 validated by Western blot, confirming effective transduction and target suppression.

155 **siNFYA transfection and JQ1 treatment**

156 NFYA-specific siRNA (Santa Cruz Biotechnology, sc-29947) and non-silencing control siRNA
157 (Santa Cruz Biotechnology, sc-37007) were purchased from Santa Cruz Biotechnology. Cells
158 were transfected with 40 nM siRNA using X-tremeGENE 360 reagent (Roche, 8724156001)
159 following the manufacturer's protocol. After 48 hours, transfected cells were treated with JQ1 (1
160 μM for 24 hours), and NFYA knockdown efficiency was assessed by Western blot.

161 **Western blotting**

162 Cells at 80–90% confluency were scraped on ice using a cell lifter (Biologix, 70-2180) into lysis
163 buffer (50 mM Tris, pH 7.5; 150 mM NaCl; 5 mM EDTA; 1% Triton X-100) supplemented with
164 protease inhibitor cocktail (Sigma-Aldrich, SIAL-11836170001) and phosphatase inhibitor
165 cocktail (Roche, 04906837001). Lysates were incubated on ice for 30 minutes and then clarified
166 by centrifugation at 14,000 rpm for 10 minutes at 4°C. Supernatants were transferred to fresh
167 tubes, and protein concentrations were measured using the DC Protein Assay Kit (Bio-Rad;
168 Reagents A, B, S: 5000113, 5000114, 5000115). A total of 20 μg of protein was mixed with 4×
169 LDS sample buffer (Invitrogen, B0007) and 10× NuPAGE Sample Reducing Agent (Invitrogen,
170 NP0009), adjusted to a final volume of 20 μl, and heated at 70°C for 10 minutes. Samples were
171 loaded onto 4–12% Bis-Tris NuPAGE gels (Invitrogen, NP0321) and electrophoresed using a
172 Mini Gel Tank (Thermo Fisher, A25977) in MES SDS Running Buffer (Invitrogen, NP0002) at

173 120 V for 90 minutes. Proteins were transferred to 0.45 μm PVDF membranes (Millipore,
174 IPVH00010) at 350 mA for 150 minutes at 4°C. Membranes were blocked in 5% skim milk in
175 Tris-buffered saline (Bio-Rad, 1706435) with 0.1% Tween-20 (Fisher Scientific, BP337-500)
176 (TBST) for 1 hour at room temperature. They were then incubated overnight at 4°C with primary
177 antibodies (see Table S4) diluted in 5% skim milk in TBST under gentle agitation (~70 rpm)
178 (ONILAB, SK-O180-S). Following incubation, membranes were washed three times for
179 10 minutes each with 1× TBST on a rocker and then incubated with HRP-conjugated secondary
180 antibodies (see Table S4) in the blocking buffer for 1 hour at room temperature. Membranes
181 were subsequently washed three more times for 10 minutes with TBST. Signal was detected
182 using SuperSignal West Femto Maximum Sensitivity Substrate (Thermo Scientific, 34094) and
183 visualized using the Amersham Imager 600 (GE Healthcare Life Sciences). Knockdown
184 efficiency was quantified in ImageJ using the Gel Analysis tool by measuring band intensities
185 (area under the curve). Target protein levels were normalized to the loading control and
186 expressed relative to shScr for each cell line.

187 **Animal studies and treatment regimen**

188 Female athymic nude (*Nu/Nu*) mice (6 weeks old) were obtained from the Jackson Laboratory
189 (Strain #:002019) and housed under specific pathogen-free conditions in the Genome and
190 Biomedical Sciences Facility at the University of California, Davis. Mice were maintained with
191 controlled ambient temperature and a standard light–dark cycle. All procedures were approved
192 by the University of California Davis Institutional Animal Care and Use Committee (Protocol
193 #24016). JQ1 (MedChemExpress, HY-13030) was prepared by dissolving the drug in DMSO
194 (Sigma-Aldrich, 472301-500ML), then diluting in vehicle composed of 95% of a 20% SBE-β-CD
195 solution (MedChemExpress, HY-17031) in saline (Moltox, C790D04) to a final concentration of
196 5 mg/ml. For subcutaneous tumor engraftment, cells were trypsinized, passed through a 40 μm
197 cell strainer (Biologix, 15-1040), and resuspended in 50 μl of Cultrex Reduced Growth Factor

198 Basement Membrane Extract (Bio-Techne, 3533-010-02). Each mouse received 0.5×10^6 cells:
199 shScramble (shScr) control cells in the left flank and shBrd2 cells in the right flank. Three days
200 post-engraftment, mice were randomized into two treatment groups (n = 10 per group) and
201 administered either vehicle or JQ1 intraperitoneally at 50 mg/kg, once a day, five days per week.
202 Tumor size was measured using Vernier calipers three times per week, and tumor volume was
203 calculated as: $(\pi \times \text{length} \times \text{width}^2)/6$. At the end of the treatment period, mice were euthanized,
204 and tumors were harvested for histological analysis.

205 **Histology and immunohistochemistry**

206 Harvested tumors were fixed in 10% neutral buffered formalin (Fisher Scientific, 22-110-873) and
207 replaced with 70% ethanol (Thomas Scientific, C993Y81) on the following day. Formalin-fixed
208 paraffin-embedded sections with 5 μm thickness were prepared for immunohistochemistry (IHC),
209 which was performed at the Center for Genomic Pathology, University of California, Davis. For
210 Ki67 staining, antigen retrieval was performed for 45 minutes with citrate buffer at pH 6.0 in a
211 Decloaking Chamber (Biocare Medical) at 125°C and 15 psi. Slides were blocked with normal
212 goat serum then incubated with rabbit polyclonal Ki67 (NeoMarkers, RB1510P, 1:1000 dilution)
213 overnight at room temperature in a humidified chamber, followed by biotinylated goat anti-rabbit
214 secondary antibody (1:1000 dilution). The Vectastain® ABC elite kit and diaminobenzidine
215 peroxidase substrate kit (Vector Laboratories) were used for amplification and visualization of
216 signal, respectively Ki67 staining was quantified in ImageJ using the IHC Profiler plugin (15).
217 Nuclei classified as high positive or positive by the plugin were counted as Ki67-positive.

218 **RNA extraction**

219 Cells were lysed in 1 ml of TRIzol reagent (Thermo Fisher Scientific, 15596026) at room
220 temperature for 5 minutes with gentle agitation, then 200 μl of chloroform (Reagents, C755N59)
221 was added. Total RNA was purified using the PureLink RNA Mini Kit (Invitrogen, 12183018A)

222 according to the manufacturer's instructions. RNA concentration and purity were assessed using
223 a NanoDrop ND-1000 spectrophotometer (Thermo Scientific) prior to downstream applications.

224 **Reverse transcription quantitative PCR (RT-qPCR)**

225 Total RNA was extracted using TRIzol reagent (Invitrogen, 15596026). After 5 minutes of
226 incubation at room temperature, 200 µl of chloroform (Reagents, C755N59) was added, and
227 samples were vigorously mixed until homogeneous, followed by 5 minutes on ice. Samples were
228 centrifuged at 14,000 rpm for 15 minutes at 4°C, and the aqueous phase was transferred to a
229 new DNase/RNase-free tube. RNA was further purified using the PureLink RNA Mini Kit
230 (Invitrogen, 12183018A), including on-column DNase treatment (PureLink DNase Set,
231 Invitrogen, 12185010). RNA was eluted in nuclease-free water, and concentration and purity
232 were assessed using a NanoDrop ND-1000 spectrophotometer (Thermo Scientific).

233 cDNA synthesis was performed with the High-Capacity cDNA Reverse Transcription Kit (Applied
234 Biosystems, 4368814) using 1 µg of total RNA per 20 µl reaction. The reaction mix included 3 µl
235 10× RT buffer, 1.2 µl 25× dNTP mix, 3 µl 10× random primers, 1.5 µl MultiScribe reverse
236 transcriptase, and 6.3 µl nuclease-free water. The thermocycling conditions were: 25°C for 10
237 minutes, 37°C for 120 minutes, and 85°C for 5 minutes.

238 qPCR was performed using 1 µl of cDNA with PowerTrack SYBR Green Master Mix (Applied
239 Biosystems, A46109) and gene-specific primers (listed in Table S5) in a total reaction volume of
240 10 µl. Reactions were run on a LightCycler 480 system (Roche) with the following setting: 95°C
241 for 10 minutes, followed by 40 cycles of 95°C for 15 seconds and 60°C for 60 seconds. Relative
242 mRNA expression levels were normalized to *GAPDH* (human samples) or *Gapdh* (mouse
243 samples) and calculated using the $2^{-\Delta\Delta Ct}$ method.

244 **Chromatin immunoprecipitation assays (ChIP-seq and ChIP-qPCR)**

245 <u>BRD2 and BRD4 ChIP-seq</u> ChIP

246 was performed using the SimpleChIP® Enzymatic Chromatin IP Kit (Magnetic Beads) (Cell
247 Signaling Technology, 9003) with minor modifications. Briefly, approximately 1×10^7 mT3-2D or
248 mT23-2D cells were dissociated with TrypLE Express (Gibco, 12605028), resuspended in PBS,
249 crosslinked with 1% formaldehyde for 10 minutes at room temperature, and quenched with 125
250 mM glycine for 5 minutes. Chromatin was digested with MNase (1 µL, 37°C, 20 minutes) and
251 sonicated (Bioruptor, Diagenode) at a high power (3 rounds of 10 cycles, 30 seconds on/30
252 seconds off) to obtain ~150–900 bp fragments. A 2% input aliquot (10 µl) was reserved, and the
253 remaining chromatin was incubated overnight at 4°C with constant rotation with 10 µl of BRD2
254 (Cell Signaling Technology, 5848S) or BRD4 (Bethyl, A301-985A100) antibody per reaction.
255 Bead capture, washes, elution, reverse crosslinking, and DNA purification were performed
256 according to the kit protocol.

257 NFYA ChIP-qPCR

258 ChIP-qPCR was performed similarly using approximately 4×10^6 HEK293T cells per reaction,
259 except chromatin was digested with 0.5 µl MNase (37°C, 10 minutes) and sonicated for 6 cycles
260 (30 seconds on/30 seconds off at high power). Immunoprecipitations used 1 µl of NFYA antibody
261 (Diagenode, C15310261) or 10 µl IgG control (Cell Signaling Technology, 2729S). qPCR was
262 performed using PowerTrack SYBR Green Master Mix (Applied Biosystems, A46109) with
263 primers in Table S5, following the qPCR conditions described in the RT-qPCR section. Percent
264 input was calculated as $100 \times 2^{(\text{Ct adjusted input} - \text{Ct ChIP})}$. ChIP-seq and ChIP-qPCR were generated
265 using a single biological replicate per condition.

266 **Library preparation and sequencing**

267 Library preparation and sequencing were carried out by Novogene Co., LTD. For RNA-seq, total
268 RNA quality was assessed using 1% agarose gel electrophoresis, NanoDrop spectrophotometry,
269 and an Agilent 2100 Bioanalyzer. Poly(A) mRNA was enriched from total RNA using oligo(dT)

magnetic beads, fragmented, and reverse-transcribed to synthesize first-strand cDNA with random primers. Second-strand cDNA synthesis was performed using a dUTP-incorporation protocol to maintain strand specificity. The resulting double-stranded cDNA was end-repaired, A-tailed, and ligated to Illumina adapters, followed by size selection (250–300 bp insert) and PCR amplification. Libraries were quantified, quality-checked, and sequenced on an Illumina NovaSeq X Plus platform to generate paired-end 150 bp reads (PE150). For ChIP-seq, sample quality was assessed prior to library construction. DNA fragments were end-repaired, A-tailed, and ligated to Illumina adapters, followed by size selection, PCR amplification, and quantification. Libraries were sequenced on an Illumina NovaSeq X Plus platform (PE150). Quality control procedures, including assessments of sequencing quality distribution, error rate distribution, and AT/CG base composition, were performed before data delivery.

Bioinformatic analysis

All analyses were performed on the Galaxy platform unless otherwise stated. Raw reads were quality-trimmed with Trim Galore! to remove adapter sequences and low-quality bases.

<u>RNA-seq analysis</u>

For RNA-seq, clean reads were aligned to the *Mus musculus* mm9 reference genome using HISAT2, and gene-level counts were obtained with featureCounts. Normalization and differential expression analysis were performed with DESeq2, using the median-of-ratios method. P-values were adjusted for multiple testing using the Benjamini–Hochberg procedure, and genes with adjusted $p < 0.05$ were considered significantly differentially expressed. Normalized counts were obtained from DESeq2, annotated using annotatemyIDs, and used for downstream visualization. Volcano plots were generated by plotting the $\log_2$FC against $-\log_{10}$p-adj to highlight significantly upregulated and downregulated genes.

<u>ChIP-seq analysis</u>

294 All ChIP-seq samples were processed using the same analysis pipeline with identical parameters
295 as described below. Trimmed reads were aligned to the *Mus musculu*s mm9 reference genome
296 with Bowtie2, then filtered with SAMtools to retain only properly paired reads with a mapping
297 quality ≥ 30 while excluding mitochondrial reads (chrM). PCR and optical duplicates were
298 removed with Picard MarkDuplicates. To ensure that only high-quality, non-redundant reads
299 were used in downstream analyses, we evaluated ChIP enrichment using standard QC metrics.
300 Across all BRD2/BRD4 ChIP-seq samples, the mean mapped read depth was 17.4 million
301 reads. Enrichment assessed by FRiP averaged 0.33 across IP samples, and IP enrichment
302 relative to input was additionally supported by deepTools plotFingerprint.

303 Peaks were called with MACS2. Consensus peaks were defined as those present in both
304 biological replicates using bedtools intersect. For each cell line, BRD2/BRD4 co-occupied
305 regions were identified by intersecting BRD2 and BRD4 consensus peak sets. Regions were
306 recentered on peak summits and extended ± 2 kb to create fixed windows for signal extraction.

307 Signal coverage tracks (BigWig files) were generated from duplicate-removed BAM files using
308 bamCoverage with RPGC normalization (scaled to scaled to 1× genome coverage). Signal
309 changes across ranked regions were visualized with deepTools (plotHeatmap, plotProfile). Per-
310 region signal was extracted using deepTools computeMatrix reference-point (±2,000 bp, 50-bp
311 bins, refPoint = center, skipZeros = true, missingDataAsZero = true). For each region, bins were
312 averaged to obtain a single signal value per replicate and condition (DMSO, JQ1). Using a single
313 ChIP-seq dataset per condition, we used a rank-based, region-level analysis to summarize
314 relative signal changes and interpreted these results as descriptive.

315 To define BRD2 regions most sensitive to BET inhibition in the sensitive cell line, a per-region
316 change in mT3-2D was calculated as $\Delta = BRD2_{DMSO} - BRD2_{JQ1}$, where larger positive Δ indicates
317 greater BRD2 loss following JQ1. The top 5% mT3 JQ1-sensitive BRD2 regions (mm9
318 coordinates) were assigned to candidate genes using GREAT with the default basal-plus-

319 extension model (proximal: 5 kb upstream and 1 kb downstream of the transcription start site;
320 distal up to 1 Mb), yielding 1,035 associated genes. Functional enrichment for GO Biological
321 Process (GOBP) terms was first assessed using GREAT, and the same gene set was additionally
322 analyzed using ShinyGO GOBP (default mouse genome background; Benjamini–Hochberg FDR
323 correction; $q < 0.05$) for complementary visualization and reporting. The top 10 enriched terms
324 were reported. For integrative expression analysis, GREAT-associated genes were intersected
325 with the RNA-seq expression matrix (DESeq2-normalized counts), resulting in 1,028 genes that
326 were visualized in Morpheus as heatmaps of row-scaled z-scores (z-score computed per gene
327 across samples).

328 **Analysis of publicly available datasets**

329 <u>RNA-seq analysis of BRD2 response to BET inhibition (JQ1)</u>

330 RNA-seq expression data from human conventional cancer cell lines were obtained via the
331 GEO2R portal. Differential expression analysis was performed using the limma package as
332 implemented in GEO2R. Log_2FC and $-log_{10}$p-adj for *BRD2* were extracted to evaluate its response
333 to JQ1 treatment, and these values were visualized as dot plots in R. To visualize differential
334 expression patterns after JQ1 treatment, 3D volcano plots were generated in R (version 4.3.0)
335 using DESeq2 output from GEO2R, with specific focus on *BRD2* and *NFYA*. A summary of the
336 datasets analyzed, including GEO accession numbers, cancer types, and sample details, is
337 provided in the Table S6.

338 <u>RNA-seq analysis of BRD4 knockdown</u>

339 RNA-seq data from human conventional cancer cell lines were obtained from the GEO2R portal.
340 Normalized counts were used as provided, and BRD2 expression was compared between control
341 and BRD4 knockdown conditions. The datasets used in this analysis are listed in Table S7.

342 <u>ChIP-seq analysis of BRD2, BRD4, and NFYA</u>

BRD2 and BRD4 ChIP-seq data from human breast cancer cell lines (GSE131097) were obtained from GEO (listed in Table S8). Processed peak files (BED) and signal tracks (BigWig) were used directly from the repository. For BRD2 and BRD4 ChIP-seq, binding sites were intersected using bedtools intersect to define co-occupied regions, and signal distribution across these regions was assessed with computeMatrix followed by plotProfile to generate metaprofiles. For NFYA, H3K4me3, RNA Pol II ChIP-seq, browser tracks of each BigWig file from GEO (listed in Table S9) were visualized in IGV (version 2.13.2) at the *BRD2* locus.

Statistical analysis

All statistical analyses were performed using GraphPad Prism version 10.6.0 (796). Statistical significance between two groups was assessed using a two-tailed, unpaired Student's t-test. For comparisons involving more than two groups, one-way ANOVA with Tukey's post hoc test was used. A $p < 0.05$ was considered statistically significant. Error bars represent the SEM unless otherwise indicated.

356 **Results**

357 **BET inhibition upregulates BRD2 across cancer types**

358 To identify adaptive transcriptional responses to BET inhibition across cancer types, we first
359 performed a systematic analysis of publicly available transcriptomic data. In total, we curated 51
360 human RNA-seq datasets following treatment with a small molecule BETi JQ1 from the Gene
361 Expression Omnibus (GEO), published over the past decade (2014–2024), encompassing a wide
362 spectrum of malignancies including prostate, breast, brain, skin, gastrointestinal, lung, pediatric,
363 gynecologic and hematologic cancers (16-64). Across all datasets analyzed, *BRD2* expression
364 was consistently and significantly upregulated upon JQ1 treatment, emerging as a recurrent
365 transcriptional response to BET inhibition **(Fig. 1A)**, while no consistent induction was observed
366 for BRD3 and BRD4. The strongest increase in *BRD2* expression was observed in castration-
367 resistant prostate cancer (CRPC; GSE78213), where JQ1 treatment induced a significant
368 upregulation ($\log_2$FC = 2.15; p-adj = 0.00), whereas *BRD3* and *BRD4* exhibited only modest
369 changes ($\log_2$FC = -0.13, p-adj = 0.0931; $\log_2$FC = 0.15, p-adj = 0.561, respectively) **(Fig. 1B)**. To
370 validate the findings from the publicly available datasets, we selected cell lines from multiple
371 cancer types represented in the GEO analysis and assessed *BRD2* expression after JQ1
372 treatment. These included CRPC (PC3), hepatocellular carcinoma (HCC; Huh7), triple-negative
373 breast cancer (TNBC; MDA-MB-231 and SUM159), glioblastoma (GBM; U251), neuroblastoma
374 (NB; SK-N-BE2), non-small cell lung cancer (NSCLC; A549), osteosarcoma (OS; U2OS), mouse
375 and human acute myeloid leukemia (AML; RN2 and HL-60). In all cell lines tested, BRD2 protein
376 levels were significantly increased following JQ1 treatment **(Fig. 1C; Fig. S1A)**. Notably, BRD2
377 expression was generally low in leukemia cell lines that we tested. In human AML (HL-60), BRD2
378 was undetectable at the protein level under baseline conditions; however, we confirmed its
379 induction at the mRNA level in response to JQ1. Similarly, in mouse AML (RN2), BRD2 protein
380 became detectable only after JQ1 exposure **(Fig. S1B–S1C)**. Collectively, these findings

381 confirmed that BRD2 upregulation emerged as a universal response to BET inhibition,
382 distinguishing it from other BET family members. These results suggest a previously
383 underappreciated role for BRD2 in the context of pharmacological BET blockade and raise the
384 possibility that its upregulation reflects a feedback or compensatory mechanism.

385 **Pharmacological BET inhibition, not BRD4 depletion, induces BRD2 upregulation in**
386 **pancreatic cancer**

387 Previously, we reported that BRCA2 deficiency sensitized pancreatic ductal adenocarcinoma
388 (PDAC) cells to BETi (65), in contrast to the general resistance observed in most PDAC cells to
389 BETi. To further investigate the underlying mechanisms of *BRD2* upregulation upon BET
390 inhibition, we used PDAC as a model system. In the publicly available dataset GSE192903,
391 which profiles PANC-1 cells treated with JQ1, BRD2 was significantly upregulated ($\log_2$FC =
392 1.18, p-adj = 4.87×10^{-185}) **(Fig. 2A)**. To validate this, we treated 3 murine KPC pancreatic
393 cancer cell lines (mT3-2D, mT19-2D, and mT23-2D) with JQ1 and conducted RNA-seq. Principal
394 component analysis (PCA) revealed distinct transcriptomic shifts upon the treatment, indicating
395 that JQ1 broadly altered the transcriptional landscape **(Fig. S2A)**. In line with their transcriptional
396 activation role, JQ1 treatment led to widespread gene downregulation, with 1,839 genes
397 significantly decreased. Although *Brd3* and *Brd4* expression remained unchanged, 353 genes
398 were significantly upregulated. Notably, *Brd2* was among the most significantly induced genes
399 ($\log_2$FC = 2.25, p-adj = 7.16×10^{-25}) **(Fig. 2B)**. This finding was further validated by RT-qPCR
400 and Western blot in both murine primary and metastatic PDAC cells, along with a panel of
401 human PDAC cell lines, confirming that BRD2 upregulation is a robust and reproducible
402 transcriptional response to BET inhibition across species and disease stages **(Fig. 2C–D; Fig.**
403 **S2B–D)**. Importantly, this effect was not limited to JQ1; treatment with other small-molecule
404 BETi, including birabresib, molibresib, CPI-0610, ZEN-3694, and AZD5153, also elevated BRD2
405 protein expression **(Fig. 2E; Fig. S2E–F)**. Because BRD4 is a major BET family with well-

406 established role in transcriptional regulation, we next asked whether BRD2 upregulation could
407 be induced by genetic depletion of BRD4. To test this, we knocked down BRD4 using shRNA in
408 the same murine PDAC cell lines. Despite successfully silencing BRD4, BRD2 expression
409 remained unchanged, highlighting that BRD4 KD elicits a different transcriptional response from
410 pharmacological BET inhibition. **(Fig. 2F; Fig. S2G)**. Consistent with this observation, BRD2
411 was upregulated by JQ1 in various cancer models, but not by genetic depletion of BRD4 **(Fig.**
412 **S2H)** (47, 55, 66-69). While the transcriptomic profile of shBRD4 cells shifted in a similar
413 direction to that of JQ1-treated cells, the changes were less pronounced, indicating that BRD4
414 KD only partially phenocopies BET inhibition **(Fig. 2G)**. Together, these findings demonstrate
415 that pharmacological BET inhibition induces BRD2 upregulation as part of a broader
416 transcriptional response that is mechanistically distinct from BRD4 depletion, potentially
417 reflecting an adaptive program to preserve transcriptional output.

418 **NFYA is one of the potential upstream regulators of BRD2 in response to BET inhibition**

419 BETi-mediated induction of BRD2 prompted us to investigate the upstream factors that might be
420 linked to its regulation. Given that gene induction is often shaped by transcription factors (TF),
421 we sought to nominate TF candidates that might regulate BRD2. We began by querying the
422 COEXPRESdb platform for transcription factors co-expressed with BRD2. Among the top 30 co-
423 expressed genes, Nuclear Transcription Factor Y subunit Alpha (NFYA) was the only TF
424 identified **(Fig. S3A–B)**. Consistent with this, our analysis of transcriptomic data from DepMap
425 across 1,684 human cancer cell lines revealed a positive correlation between *NFYA* and *BRD2*
426 expression (Pearson's $r = 0.628$, $p = 0.00$) **(Fig. 3A)**. We next asked whether *NFYA* and *BRD2*
427 exhibit coordinated responses to BET inhibition. Analysis of both publicly available RNA-seq
428 datasets and our mouse PDAC dataset revealed that both *NFYA* and *BRD2* were upregulated
429 under JQ1 treatment **(Fig. 3B; Fig. S3C)**. To evaluate whether NFYA acts as an upstream
430 regulator of *BRD2* transcription, we analyzed public NFYA ChIP-seq datasets and observed

431 NFYA signal near the *BRD2* transcription start site (TSS) within an active promoter region
432 marked by H3K4me3 and RNA Pol II occupancy across multiple cell types **(Fig. 3C; Fig. S3D)**.
433 To test this relationship, we performed siRNA-mediated KD of NFYA in HEK293T and U2OS
434 cells. Depletion of NFYA reduced basal levels of *BRD2* expression and partially reduced BRD2
435 expression after JQ1 treatment **(Fig. 3D–G; Fig. S3E–F)**. Indeed, NFYA ChIP-qPCR showed
436 the increased NFYA binding at the BRD2 promoter region upon JQ1 treatment relative to IgG
437 control **(Fig. S3D)**, suggesting that NFYA may contribute, at least in part, to *BRD2* transcriptional
438 upregulation in response to BET inhibition.

439 **BRD2 knockdown sensitizes cells to BET inhibition *in vitro***

440 Given the robust upregulation of BRD2 following BET inhibition, we hypothesized that BRD2
441 upregulation might confer adaptive resistance to BETi. To test this, we performed shRNA-
442 mediated KD of BRD2 in a panel of cancer cell lines and evaluated their sensitivity to BETi. In
443 mouse PDAC cells, BRD2 KD enhanced sensitivity to 6 different BETi—JQ1, birabresib,
444 molibresib, ZEN-3694, CPI-0610, and AZD5153 **(Fig. 4A–B)**. Similar results were also observed
445 in 3 additional human cancer cell lines—A549 (NSCLC), U251 (GBM), and U2OS (OS)—where
446 BRD2 KD consistently increased JQ1 sensitivity **(Fig. 4C–H)**. Across multiple cell lines, BRD2
447 depletion sensitized cells to BET inhibition, supporting that BRD2 upregulation contributes to
448 adaptive resistance against BET inhibition **(Fig. S4A–I)**. Moreover, clonogenic assays under
449 chronic treatment mirrored this response, with durable suppression of colony outgrowth over
450 extended BETi exposure **(Fig. S4J–O)**. Interestingly, we observed that the magnitude of
451 sensitization varied depending on the cell's initial response to BETi. Cells that were more
452 resistant to BET inhibition at baseline (mT23-2D, mM1-2D, mM6-2D, and Capan-2) exhibited a
453 greater reduction in IC_{50} upon BRD2 KD compared to those that were initially sensitive (mT3-2D,
454 CFPAC-1, and BxPC3) **(Fig. 4I–N, Fig. S4A–I)**. In sum, our results revealed a functional role for

455 BRD2 in mediating an acute adaptive response to BETi, suggesting that targeting BRD2
456 enhances therapeutic efficacy, particularly in BETi-resistant tumors.

457 **BRD2 depletion enhances BETi efficacy *in vivo***

458 To evaluate whether BRD2 contributes to BETi response *in vivo*, we subcutaneously injected
459 mouse pancreatic cancer cells (mT23-2D) harboring control or BRD2-targeting shRNA into
460 immunocompromised athymic *Nu/Nu* mice. Mice were treated intraperitoneally with either
461 vehicle or JQ1 (50 mg/kg) over a three-week period **(Fig. 5A)**. While both JQ1 treatment alone
462 or BRD2 KD alone moderately suppressed tumor growth, combined BRD2 KD and JQ1
463 treatment resulted in striking tumor growth suppression **(Fig. 5B–D)**. No overt toxicity was
464 observed as body weight remained stable across treatment arms **(Fig. S5)**. Immunohistochemical
465 analysis of Ki67 staining revealed a marked reduction in proliferative cells in BRD2 KD tumors
466 treated with JQ1, which exhibited the lowest percentage of Ki67-positive cells **(Fig. 5E–F)**.
467 Together, these results demonstrate that BRD2 depletion significantly enhances the antitumor
468 efficacy of BET inhibition *in vivo*.

469 **BRD2 persists on chromatin preferentially in BETi-resistant cells**

470 Given our findings that BRD2 is associated with adaptive resistance to BET inhibition both *in vitro*
471 and *in vivo*, we sought to investigate potential underlying mechanisms. We first examined the
472 basal expression levels of BRD4 and BRD2 but did not observe a clear correlation with JQ1 IC_{50}
473 values **(Fig. S6A–B)**, consistent with DepMap data across 394 cell lines (Pearson's r = -0.102
474 and -0.058 for BRD4 and BRD2, respectively) **(Fig. S6C–D)**. Since BETi displaces BET proteins
475 from acetylated chromatin, we hypothesized that differential BETi responses between BETi-
476 sensitive (mT3-2D) and BETi-resistant (mT23-2D) cells **(Fig. 6A; Fig. S6E)** may reflect differential
477 BRD2 and BRD4 chromatin occupancy after BETi treatment. To address this, we performed BRD2
478 and BRD4 ChIP-seq in both BETi-sensitive (mT3-2D) and BETi-resistant (mT23-2D) cells to

479 compare their chromatin occupancy under DMSO and JQ1 conditions. In the DMSO condition,
480 we identified common BRD4 (n = 24,810) and BRD2 peaks (n = 23,706) between these two cell
481 lines. Notably, about 70% of BRD4-bound regions (16,941 of 24,810 peaks) were also bound by
482 BRD2 **(Fig. 6B)**. In these overlapping regions, upon JQ1 treatment, we found that BRD4
483 chromatin occupancy overall decreased in both cell lines to a similar extent. However, BRD2
484 occupancy was retained to a greater degree in BETi-resistant (mT23-2D) cells than BETi-sensitive
485 (mT3-2D) cells **(Fig. 6C)**. A similar pattern of BRD2 persistence has been observed in TNBC cell
486 line (SUM149) after BET inhibition, suggesting a broader relevance across cancer types **(Fig.**
487 **S6F–G)**. To further examine whether differential BRD2 displacement affects transcriptional output,
488 we focused on the top 5% of BRD2/BRD4 co-occupied sites showing the greatest loss of BRD2
489 binding after JQ1 treatment in mT3-2D cells (847 regions), which were comparatively better
490 preserved in JQ1-treated mT23-2D cells. Consistent with this binding pattern, our RNA-seq
491 analysis revealed a more pronounced transcriptional shift for genes associated with these sites
492 in mT3-2D cells, whereas the corresponding transcriptional profiles in mT23-2D cells remained
493 closer to DMSO-treated controls **(Fig. 6D)**. Gene ontology analysis of this gene set showed
494 enrichment for chromatin organization/modification and RNA processing programs, suggesting
495 potential roles of these genes in mediating adaptive resistance of BETi **(Fig. 6E; Fig. S6H)**.
496 Collectively, our data support a model in which, upon BET inhibition, resistant behavior is
497 associated with greater BRD2 chromatin retention and more preserved transcriptional output
498 despite reduced BRD4 occupancy **(Fig. 6F)**. These findings suggest that BRD2 may serve as a
499 compensatory factor when BRD4 is displaced from chromatin and provide a rationale for targeting
500 BRD2 in combination with BETi to improve therapeutic responses.

501 **Discussion**

502 BRD4 dependency in many cancers, including leukemia, provided the rationale for developing
503 BETi. The first-generation inhibitor JQ1 demonstrated potent antitumor effects in preclinical

504 models such as NUT carcinoma and MYC-driven leukemia. However, its poor bioavailability,
505 short half-life, and off-target toxicities limited its clinical use, prompting the development of
506 second-generation BETi with improved pharmacokinetics, enhanced specificity, and orally
507 available formulations. Indisputably, despite these advances, cancer cells can activate
508 alternative pathways to circumvent therapy, mitigating its effects and sustaining survival. These
509 adaptive responses not only represent tangible vulnerabilities but, when understood, can also
510 be exploited to prevent resistance and achieve better therapeutic outcomes. Several studies
511 have informally noted increased BRD2 expression following BETi treatment, but it has remained
512 unclear whether this functionally confers pan-cancer adaptive resistance. Recent synthetic lethal
513 screens with BETi in TNBC and paralog-focused CRISPR screens in lung, skin, pancreas, and
514 brain cancers have independently identified BRD2 as a potential resistance factor (70, 71). Yet,
515 the role of BRD2 has not been systematically examined. Here, we show that transcriptional
516 upregulation of BRD2 is a robust adaptive response to BETi across diverse cancer types, and
517 that BRD2 depletion sensitizes cells to BET inhibition both *in vitro* and *in vivo*.

518 Paralog compensation is an emerging theme in targeted cancer therapy, wherein inhibition of
519 one protein prompts adaptive upregulation of a closely related family member that compensates
520 for its function. For example, EZH2 inhibition in malignant rhabdoid tumors has been shown to
521 induce EZH1 upregulation, and dual EZH1/2 inhibition yields improved therapeutic responses
522 (72). Similarly, inhibition of the histone demethylase LSD1 (KDM1A) in Ewing sarcoma cells
523 resulted in marked induction of its homolog LSD2 (KDM1B), a shift that modulates drug
524 sensitivity (73). Recent large-scale paralog-focused CRISPR screens have uncovered multiple
525 additional examples of this phenomenon, such as the reciprocal buffering between DUSP4 and
526 DUSP6 (71). Here, we present the first comprehensive evidence that BRD2 upregulation is a
527 highly conserved and universal adaptive response to BET inhibition across cancer types,

528 functionally analogous to other paralog compensation events in which BRD2 substitutes for
529 BRD4 to preserve transcriptional programs upon BET inhibition.

530 Our data suggest that resistance is mediated in part through paralog redundancy, with BRD2
531 compensating for BRD4 function under BET inhibition. This compensatory role aligns with their
532 shared canonical functions in transcriptional regulation, as evidenced by their largely overlapping
533 genomic occupancy (70). However, BRD2 also carries out distinct functions that may
534 independently and uniquely support adaptive resistance. Upon JQ1 treatment, BET proteins can
535 remain in the nucleus and, through their extra-terminal (ET) domains, may exert bromodomain-
536 independent functions that sustain cell survival. Unlike BRD4, BRD2 is closely associated with
537 chromatin architectural regulation: it co-localizes genome-wide with CTCF, contributes to the
538 maintenance of topologically associating domain (TAD) boundaries, and influences
539 compartmentalization of the accessible genome (74, 75). The C-terminal domain of BRD2 also
540 mediates critical protein-protein interactions, enabling its recruitment to promoters and CTCF-
541 bound sites. The unique roles of BRD2 raise the possibility that its upregulation under BET
542 inhibition may confer survival advantages beyond its role in transcriptional regulation.

543 Our findings suggest a therapeutic opportunity to enhance BETi efficacy by preventing or
544 counteracting BRD2 upregulation. This could be achieved either through selective BRD2
545 inhibition in combination with conventional BETi which predominantly target BRD4 or by
546 strategies that broadly degrade BET family members to prevent compensatory mechanisms.
547 PROTAC-based BET degraders, which remove BRD2, BRD3, and BRD4 from chromatin, have
548 recently demonstrated superior antitumor activity compared to earlier generations of BETi (59,
549 76). Notably, the absence of BRD2 upregulation in PROTAC-based approaches may partially
550 explain their improved efficacy. While additional resistance mechanisms undoubtedly exist, our
551 data highlight BRD2 compensation as a conserved and targetable pathway. As a proof-of-
552 principle, we show that BRD2 depletion sensitizes tumors to BET inhibition. This provides a

553 rationale for integrating BETi with approaches that mitigate BRD2-driven adaptive resistance to
554 achieve more durable clinical responses and expand the therapeutic potential of BET-targeted
555 strategies in cancer therapeutics.

556 **Figure legends**

557 **Fig. 1 Pan-cancer BRD2 upregulation upon BET inhibition. (A)** Dot plots showing *BRD2*
558 expression changes (JQ1 vs. control) across 51 curated human RNA-seq datasets from GEO
559 (2014–2024), including gastrointestinal, breast, prostate, skin, brain, lung, pediatric, gynecologic,
560 and hematologic cancers. The x-axis represents log_2fold change (log_2FC), and dot size
561 corresponds to statistical significance (-log_{10}p-adj). Abbreviations: CRPC, castration-resistant
562 prostate cancer; TNBC, triple-negative breast cancer; Lum A, luminal A; BC, breast cancer;
563 GBM, glioblastoma; NB, neuroblastoma; MEL, melanoma; HNSCC, head and neck squamous
564 cell carcinoma; CRC, colorectal cancer; PDAC, pancreatic ductal adenocarcinoma; GIST,
565 gastrointestinal stromal tumor; HCC, hepatocellular carcinoma; SCLC, small cell lung cancer;
566 NSCLC, non-small cell lung cancer; RMS, rhabdomyosarcoma; AT/RT, atypical teratoid/rhabdoid
567 tumor; ES, Ewing sarcoma; OC, ovarian cancer; CC, cervical cancer; MM, multiple myeloma; T-
568 ALL, T-cell acute lymphoblastic leukemia; CML, chronic myeloid leukemia; BL, Burkitt lymphoma;
569 AML, acute myeloid leukemia. **(B)** Volcano plot of differentially expressed genes in CRPC
570 (GSE78213), highlighting robust *BRD2* upregulation upon JQ1 treatment. *BRD3* and *BRD4*
571 remained unaffected. **(C)** Western blot validation showing BRD2 protein levels in multiple
572 representative human cell lines from prostate (PC3), liver (Huh7), breast (MDA-MB-231), brain
573 (U251), lung (A549), and pediatric (U2OS) cancers with and without JQ1.

574 **Fig. 2 Pharmacological BET inhibition uniquely drives BRD2 upregulation in pancreatic**
575 **cancer. (A)** Volcano plot of differentially expressed genes in human PDAC (GSE192903) treated
576 with JQ1, highlighting strong upregulation of *BRD2*, neither *BRD3* nor *BRD4*. **(B)** Volcano plot of
577 RNA-seq data from murine PDAC cells treated with JQ1, showing conserved and significant
578 upregulation of *Brd2*. **(C)** Western blot validation of BRD2 upregulation in murine PDAC cell
579 lines treated with JQ1. **(D)** Western blot analysis in a panel of human PDAC cell lines confirming
580 JQ1-induced BRD2 expression. **(E)** Western blot analysis of BRD2 in murine PDAC cells (mT23-

581 2D) treated with different small-molecule BET inhibitors, showing a consistent increase in BRD2
582 expression across inhibitors. **(F)** Western blot analysis of BRD2 expression following shRNA-
583 mediated BRD4 knockdown (KD) in murine and human PDAC cell lines, revealing that BRD4
584 depletion does not mimic JQ1-induced BRD2 upregulation. **(G)** Principal component analysis
585 (PCA) of RNA-seq data from murine PDAC cells under DMSO, JQ1, shScramble (shScr), or
586 shBrd4 conditions, showing distinct transcriptional clustering of JQ1-treated samples compared
587 to BRD4 KD.

588 **Fig. 3 NFYA as a potential candidate transcriptional factor associated with BRD2 induction**
589 **upon BET inhibition. (A)** Scatter plot from DepMap analysis showing a positive correlation
590 between *NFYA* and *BRD2* expression across public cancer transcriptomes. **(B)** Representative
591 3D volcano plot of publicly available RNA-seq datasets treated with JQ1, highlighting co-
592 upregulation of *BRD2* and *NFYA*. **(C)** NFYA ChIP-seq profiles at the *BRD2* locus across multiple
593 cell types. **(D,E)** Western blot analysis of NFYA and BRD2 in HEK293T (D) and U2OS (E) cells
594 transfected with control siRNA (siNeg) or NFYA siRNA (siNFYA) and treated with DMSO or JQ1.
595 **(F,G)** RT-qPCR analysis of *BRD2* expression in HEK293T (F) and U2OS (G) cells under the same
596 conditions, showing that NFYA KD attenuated JQ1-mediated *BRD2* upregulation. Statistical
597 significance was determined by one-way ANOVA (*$p < 0.05$, **$p < 0.01$, ***$p < 0.001$, ****$p <$
598 0.0001).

599 **Fig. 4 BRD2 depletion sensitizes cancer cells to BET inhibition. (A)** Immunoblot confirming
600 BRD2 KD (shBRD2 #1) in mT23-2D PDAC cells. Values indicate relative BRD2 protein levels
601 quantified by densitometry, normalized to GAPDH, and expressed relative to shScr. **(B)** Dose–
602 response curves showing reduced cell viability upon treatment with the indicated BETi in BRD2-
603 depleted mT23-2D cells compared to shScr controls. **(C–N)** Immunoblots confirming BRD2 KD
604 (shBRD2 #1) and JQ1 dose–response curves in lung (A549), brain (U251), pediatric (U2OS), and
605 human PDAC (Capan-2, CFPAC-1, and BxPC-3) cell lines following BRD2 KD.

606 **Fig. 5 Genetic BRD2 perturbation enhances the antitumor effect of BET inhibition *in vivo*.**
607 **(A)** Schematic of *in vivo* experimental design, created with BioRender. **(B)** Representative images
608 of mice and excised tumors from each group after treatment. Scale bar, 1 cm. **(C)** Tumor growth
609 curves over time showing significantly impaired tumor growth in shBrd2 + JQ1 tumors compared
610 to controls. Error bars represent SD. **(D)** Tumor weight at endpoint, showing that shBrd2 + JQ1
611 tumors had the lowest weights. Statistical significance was determined by two-tailed Student's t-
612 test (****$p < 0.0001$). **(E–F)** Representative Ki67 immunohistochemistry and quantification
613 showing significantly reduced proliferative index in shBrd2 + JQ1 tumors compared to controls.
614 Statistical significance was determined using two-tailed Student's t-test (****$p < 0.0001$). Scale
615 bar, 100 μm.

616 **Fig. 6 BRD2 chromatin retention may help maintain transcriptional programs in BETi-**
617 **resistant pancreatic cancer cells. (A)** Dose–response curves comparing sensitivity to BET
618 inhibitors in BETi-sensitive (mT3-2D) and JQ1-resistant (mT23-2D) PDAC cells. **(B)** Venn
619 diagram showing overlap between BRD4 and BRD2 ChIP-seq peaks across BETi-sensitive
620 (mT3-2D) and BETi-resistant (mT23-2D) cells. **(C)** Metaplots and heatmaps of BRD4 and BRD2
621 ChIP-seq signal at BRD2/BRD4-overlapping peaks (16,941 regions) in BETi-sensitive (mT3-2D)
622 and BETi-resistant (mT23-2D) cells treated with DMSO or JQ1. **(D)** RNA-seq heatmap (row-
623 scaled z-scores) and BRD2 ChIP-seq browser tracks at representative loci in both BETi-
624 sensitive (mT3-2D) and BETi-resistant (mT23-2D) cells **(E)** GREAT gene ontology enrichment
625 for genes associated with top 5% BRD2-loss sites after JQ1 in mT3-2D cells. **(F)** Proposed
626 schematic model illustrating BRD2 upregulation as an adaptive mechanism to BET inhibition.

627 **Supplementary figure legends**

628 **Supplementary Fig. 1 BRD2 upregulation by JQ1 across additional cancer types. (A)**
629 Western blot analysis of BRD2 in brain and breast cancer cells treated with DMSO or JQ1. **(B–C)**

630 RT-qPCR and immunoblot analysis of BRD2 expression in human and mouse blood cancer cells,
631 showing increased BRD2 levels upon JQ1 treatment (1 μM, 24 hours).

632 **Supplementary Fig. 2 BRD2 induction by BET inhibition but not by BRD4 KD. (A)** PCA of
633 RNA-seq profiles from three different murine PDAC cell lines treated with DMSO or JQ1, showing
634 distinct clustering of JQ1-treated samples. **(B)** RT-qPCR analysis of *BRD2* expression in multiple
635 murine and human PDAC cell lines treated with JQ1, revealing significant induction across
636 models. Statistical significance was determined using a two-tailed Student's t-test (***$p < 0.001$,
637 ****$p < 0.0001$) **(C–D)** Western blot analysis of BRD2 and BRD4 expression in murine (mT3-2D,
638 mM1-2D) and human (BxPC-3, Capan-1) PDAC cells after JQ1 treatment. **(E)** Immunoblot
639 analysis of BRD2 and BRD4 expression following treatment with JQ1, Birabresib or Molibresib in
640 mouse PDAC cells (mT3-2D and mT19-2D). **(F)** Western blot analysis of BRD2 expression in
641 murine PDAC cell lines (mT4-2D, mT5-2D, and mT8-2D) treated with different BETi (JQ1,
642 Birabresib, Molibresib, ZEN-3694, CPI-0610, AZD5153), showing consistent BRD2 upregulation
643 across inhibitors compared to control. **(G)** Western blot analysis of BRD2 expression after shRNA-
644 mediated BRD4 KD in PDAC AsPC-1 and breast cancer SUM159 cells, showing that BRD4
645 depletion did not result in BRD2 induction by JQ1. **(H)** Analysis of publicly available RNA-seq
646 datasets (GEO) across multiple cancer types, showing that BRD4 KD generally did not increase
647 *BRD2* expression, whereas JQ1 significantly induced *BRD2*. Statistical significance was
648 determined by two-tailed Student's t-test (**$p < 0.01$).

649 **Supplementary Fig. 3 NFYA emerges as a candidate regulator of BRD2. (A)** List of top 30
650 BRD2-interacting transcriptional regulators identified from COEXPRESdb. **(B)** Co-expression
651 analysis of NFYA and BRD2 using COEXPRESdb, showing a strong positive correlation across
652 transcriptomes ($z = 5.62$). **(C)** RNA-seq analysis of *Nfya* expression in mouse PDAC cells treated
653 with DMSO or JQ1, showing significant *Nfya* upregulation upon JQ1 treatment. Statistical
654 significance was determined by two-tailed Student's t-test (***$p < 0.001$). **(D)** Public ChIP-seq

655 tracks showing H3K4me3, RNA pol II, and NFYA binding across multiple cell types at the BRD2
656 locus. Lower panels: NFYA ChIP-qPCR in HEK293T cells under DMSO or JQ1 treatment showing
657 enrichment at the *BRD2* exon 1 region relative to IgG and an intergenic negative control.
658 Statistical significance was determined by two-tailed Student's t-test (**$p < 0.01$). **(E–F)** Western
659 blot analyses showing NFYA and BRD2 expression in control (shScr) and NFYA- KD (shNfya)
660 murine PDAC lines mT5-2D (E) and mT23-2D (F) following DMSO or JQ1 treatment. NFYA
661 depletion reduces BRD2 induction upon BET inhibition, which is consistent with human cell line
662 data.

663 **Supplementary Fig. 4 BRD2 KD enhances sensitivity to BET inhibition across murine**
664 **PDAC models. (A–H)** Immunoblots validating BRD2 KD using independent shRNA constructs
665 (shBrd2 #1 and/or shBrd2 #2, as indicated) and dose–response curves for BETi showing reduced
666 cell viability in BRD2-depleted cells compared with shScr controls in mouse PDAC cell lines. **(I)**
667 Table of dose–response analyses showing $LogIC_{50}$ values with 95% confidence intervals (CI) and
668 $\Delta LogIC_{50}$ values for BETi sensitivity following BRD2 KD across cell lines ($\Delta LogIC_{50}$ calculated
669 relative to shScr within each cell line). **(J–O)** Representative colony formation assays and their
670 quantification (colony area and staining intensity) in mouse PDAC cell lines.

671 **Supplementary Fig. 5 Body weight of mice was maintained during JQ1 treatment. (A)** No
672 significant weight loss was observed in mice bearing tumors treated with vehicle or JQ1.

673 **Supplementary Fig. 6 Basal BRD4/BRD2 levels and chromatin occupancy do not predict**
674 **JQ1 response. (A–B)** Correlation analyses between basal BRD4 (A) or BRD2 (B) protein
675 expression levels and JQ1 sensitivity across human PDAC cell lines. No significant associations
676 were observed. **(C–D)** Correlation of *BRD4* and *BRD2* mRNA expression levels with JQ1
677 sensitivity across public cancer transcriptome datasets. Both factors showed weak or no
678 predictive value. **(E)** Summary table of $LogIC_{50}$ and 95% CI for JQ1, Molibresib, and Birabresib
679 in BETi-sensitive (mT3-2D) and BETi-resistant (mT23-2D) cells. **(F)** Venn diagram of BRD2 and

680 BRD4 ChIP-seq binding regions in TNBC (GSE131097, SUM149), highlighting substantial
681 overlap in line with our PDAC findings. **(G)** Metaprofiles of BRD4 (left) and BRD2 (right)
682 occupancy at BRD4-bound sites under DMSO or JQ1 conditions, suggesting BRD2 binding
683 persists at regions where BRD4 occupancy is displaced upon JQ1. **(H)** GOBP enrichment
684 analysis (ShinyGO) of the top 1,000 JQ1-responsive BRD2-bound regions annotated by GREAT,
685 revealing significant enrichment for RNA metabolic and biosynthetic processes.

686 **Conclusions**

687 Our study uncovered BRD2 upregulation as a conserved adaptive resistance mechanism to BET
688 inhibition across diverse cancer types. Through integrated transcriptomic and epigenomic
689 analyses, we demonstrated that BETi treatment induced BRD2 expression at the transcriptional
690 level, at least in part mediated by the NFYA transcription factor. BETi-mediated BRD2 induction
691 acts as a compensatory mechanism, diminishing the antitumor efficacy of BETi. Notably, BRD2
692 KD sensitizes cancer cells to BETi, suggesting the therapeutic potential of dual targeting
693 strategies that inhibit BRD2 alongside BETi to improve patient outcomes across multiple cancer
694 types.

695 **Abbreviations**

696 ***AML***: acute myeloid leukemia

697 ***AT/RT***: atypical teratoid/rhabdoid tumor

698 ***BC***: breast cancer

699 ***BET***: bromodomain and extra-terminal domain

700 ***BETi***: BET inhibitors

701 ***BL***: Burkitt lymphoma

702 ***CC***: cervical cancer

703 ***CML***: chronic myeloid leukemia

704 ***CRC***: colorectal cancer

705 ***CRPC***: castration-resistant prostate cancer

706 ***ES***: Ewing sarcoma

707 ***ET***: extra-terminal

708 ***GBM***: glioblastoma

709 ***GIST***: gastrointestinal stromal tumor

710 ***HCC***: hepatocellular carcinoma

711 ***HNSCC***: head and neck squamous cell carcinoma

712 ***KD***: knockdown

713 ***Lum A***: luminal A

714 ***MEL***: melanoma

715 ***MM***: multiple myeloma

716 ***NB***: neuroblastoma

717 ***NFYA***: Nuclear Transcription Factor Y subunit Alpha

718 ***NSCLC***: non-small cell lung cancer

719 ***OC***: ovarian cancer

720 ***PDAC***: pancreatic ductal adenocarcinoma

721 ***RMS***: rhabdomyosarcoma

722 ***SCLC***: small cell lung cancer

723 ***SE***: super-enhancers

724 ***TAD***: topologically associating domain

725 ***T-ALL***: T-cell acute lymphoblastic leukemia

726 ***TF***: transcription factors

727 ***TNBC***: triple-negative breast cancer

728 **Declarations**

729 Ethics approval and consent to participate

730 All animal studies were conducted in accordance with institutional and national guidelines and
731 approved by the University of California, Davis (UC Davis) Institutional Animal Care and Use
732 Committee (IACUC; Protocol #24016, approved August 22, 2024). UC Davis is accredited by the
733 Association for Assessment and Accreditation of Laboratory Animal Care International (AAALAC)
734 and maintains an Animal Welfare Assurance with the Office of Laboratory Animal Welfare (OLAW;
735 Assurance Number D16-00272, A3433-01).

736 Consent for publication

737 All authors have reviewed and approved this manuscript and consent to its publication.

738 Availability of data and material

739 Raw and processed RNA-seq and ChIP-seq data generated in this study are available in GEO
740 under accession numbers GSE307284 (RNA-seq) and GSE307285 (ChIP-seq).

741 Competing interests

742 The authors have no conflicts of interest to disclose.

743 Funding

744 This work was supported by the National Cancer Institute grant 5R37CA249007.

745 Authors' contributions

746 S.A. and C.I.H. conceptualized and designed the study. S.A., J.J., and E.L. performed the
747 experiments and analyzed the data. S.A. drafted the original manuscript, and C.I.H. reviewed and
748 edited the manuscript. All authors read and approved the final version of the manuscript.

749 Acknowledgements

750 This study was supported by National Cancer Institute grant 5R37CA249007 (C.-I.H.). The
751 authors thank all members of the Hwang lab for their support throughout the course of this study,
752 particularly Jihao Xu and Minh Duc Pham for their valuable discussions. The authors are also
753 grateful to Dr. Chayarndorn Phumsatitpong for assistance with imaging the tumor and to Kedi
754 Huang for help in optimizing the R code for generating the 3D volcano plot. S.A. was supported
755 by the Anandamahidol Foundation (Thailand) and University of California Davis Comprehensive
756 Cancer Center Director's Fellowship. J.J. was supported by Provost's Undergraduate Fellowship.

757 **Authors' information**

758 Authors and affiliations

759 Department of Microbiology and Molecular Genetics, College of Biological Sciences, University
760 of California, Davis, Davis, CA, United States

761 University of California Davis Comprehensive Cancer Center, Sacramento, CA, United States

762 Corresponding author

763 Correspondence to Chang-il Hwang

764 **References**

765 1. Hanahan D, Weinberg RA. Hallmarks of cancer: the next generation. Cell.
766 2011;144(5):646–74.
767 2. Hanahan D. Hallmarks of Cancer: New Dimensions. Cancer Discov. 2022;12(1):31–46.
768 3. Bradner JE, Hnisz D, Young RA. Transcriptional Addiction in Cancer. Cell.
769 2017;168(4):629–43.
770 4. Shi J, Vakoc CR. The mechanisms behind the therapeutic activity of BET bromodomain
771 inhibition. Mol Cell. 2014;54(5):728–36.
772 5. Dhalluin C, Carlson JE, Zeng L, He C, Aggarwal AK, Zhou MM. Structure and ligand of a
773 histone acetyltransferase bromodomain. Nature. 1999;399(6735):491–6.
774 6. Loven J, Hoke HA, Lin CY, Lau A, Orlando DA, Vakoc CR, et al. Selective inhibition of
775 tumor oncogenes by disruption of super-enhancers. Cell. 2013;153(2):320–34.
776 7. Jang MK, Mochizuki K, Zhou M, Jeong HS, Brady JN, Ozato K. The bromodomain
777 protein Brd4 is a positive regulatory component of P-TEFb and stimulates RNA polymerase II-
778 dependent transcription. Mol Cell. 2005;19(4):523–34.
779 8. Filippakopoulos P, Qi J, Picaud S, Shen Y, Smith WB, Fedorov O, et al. Selective
780 inhibition of BET bromodomains. Nature. 2010;468(7327):1067–73.
781 9. Zuber J, Shi J, Wang E, Rappaport AR, Herrmann H, Sison EA, et al. RNAi screen
782 identifies Brd4 as a therapeutic target in acute myeloid leukaemia. Nature. 2011;478(7370):524–
783 8.
784 10. Delmore JE, Issa GC, Lemieux ME, Rahl PB, Shi J, Jacobs HM, et al. BET
785 bromodomain inhibition as a therapeutic strategy to target c-Myc. Cell. 2011;146(6):904–17.
786 11. Roe JS, Mercan F, Rivera K, Pappin DJ, Vakoc CR. BET Bromodomain Inhibition
787 Suppresses the Function of Hematopoietic Transcription Factors in Acute Myeloid Leukemia.
788 Mol Cell. 2015;58(6):1028–39.
789 12. Berthon C, Raffoux E, Thomas X, Vey N, Gomez-Roca C, Yee K, et al. Bromodomain
790 inhibitor OTX015 in patients with acute leukaemia: a dose-escalation, phase 1 study. Lancet
791 Haematol. 2016;3(4):e186–95.
792 13. Braun T, Gardin C. Investigational BET bromodomain protein inhibitors in early stage
793 clinical trials for acute myelogenous leukemia (AML). Expert Opin Investig Drugs.
794 2017;26(7):803–11.
795 14. Khandekar D, Tiriveedhi V. Role of BET Inhibitors in Triple Negative Breast Cancers.
796 Cancers (Basel). 2020;12(4).
797 15. Varghese F, Bukhari AB, Malhotra R, De A. IHC Profiler: an open source plugin for the
798 quantitative evaluation and automated scoring of immunohistochemistry images of human
799 tissue samples. PLoS One. 2014;9(5):e96801.
800 16. Zhang P, Wang D, Zhao Y, Ren S, Gao K, Ye Z, et al. Intrinsic BET inhibitor resistance in
801 SPOP-mutated prostate cancer is mediated by BET protein stabilization and AKT-mTORC1
802 activation. Nat Med. 2017;23(9):1055–62.
803 17. Coleman DJ, Van Hook K, King CJ, Schwartzman J, Lisac R, Urrutia J, et al. Cellular
804 androgen content influences enzalutamide agonism of F877L mutant androgen receptor.
805 Oncotarget. 2016;7(26):40690–703.
806 18. Kim DH, Sun D, Storck WK, Welker Leng K, Jenkins C, Coleman DJ, et al. BET
807 Bromodomain Inhibition Blocks an AR-Repressed, E2F1-Activated Treatment-Emergent
808 Neuroendocrine Prostate Cancer Lineage Plasticity Program. Clin Cancer Res.
809 2021;27(17):4923–36.
810 19. Welti J, Sharp A, Brooks N, Yuan W, McNair C, Chand SN, et al. Targeting the p300/CBP
811 Axis in Lethal Prostate Cancer. Cancer Discov. 2021;11(5):1118–37.

20. Mao W, Ghasemzadeh A, Freeman ZT, Obradovic A, Chaimowitz MG, Nirschl TR, et al. Immunogenicity of prostate cancer is augmented by BET bromodomain inhibition. J Immunother Cancer. 2019;7(1):277.
21. Liu B, Liu X, Han L, Chen X, Wu X, Wu J, et al. BRD4-directed super-enhancer organization of transcription repression programs links to chemotherapeutic efficacy in breast cancer. Proc Natl Acad Sci U S A. 2022;119(6).
22. Zanconato F, Battilana G, Forcato M, Filippi L, Azzolin L, Manfrin A, et al. Transcriptional addiction in cancer cells is mediated by YAP/TAZ through BRD4. Nat Med. 2018;24(10):1599–610.
23. Lu X, Peng L, Ding J, Li Y, Li Q, Rao M, et al. A deregulated m(6)A writer complex axis driven by BRD4 confers an epitranscriptomic vulnerability in combined DNA repair-targeted therapy. Proc Natl Acad Sci U S A. 2023;120(41):e2304534120.
24. Shu S, Lin CY, He HH, Witwicki RM, Tabassum DP, Roberts JM, et al. Response and resistance to BET bromodomain inhibitors in triple-negative breast cancer. Nature. 2016;529(7586):413–7.
25. Nagarajan S, Rao SV, Sutton J, Cheeseman D, Dunn S, Papachristou EK, et al. ARID1A influences HDAC1/BRD4 activity, intrinsic proliferative capacity and breast cancer treatment response. Nat Genet. 2020;52(2):187–97.
26. Vinik Y, Maimon A, Raj H, Dubey V, Geist F, Wienke D, et al. Computational pipeline predicting cell death suppressors as targets for cancer therapy. iScience. 2024;27(9):110859.
27. Bevill SM, Olivares-Quintero JF, Sciaky N, Golitz BT, Singh D, Beltran AS, et al. GSK2801, a BAZ2/BRD9 Bromodomain Inhibitor, Synergizes with BET Inhibitors to Induce Apoptosis in Triple-Negative Breast Cancer. Mol Cancer Res. 2019;17(7):1503–18.
28. Ren C, Zhang G, Han F, Fu S, Cao Y, Zhang F, et al. Spatially constrained tandem bromodomain inhibition bolsters sustained repression of BRD4 transcriptional activity for TNBC cell growth. Proc Natl Acad Sci U S A. 2018;115(31):7949–54.
29. Murakami S, Li R, Nagari A, Chae M, Camacho CV, Kraus WL. Distinct Roles for BET Family Members in Estrogen Receptor alpha Enhancer Function and Gene Regulation in Breast Cancer Cells. Mol Cancer Res. 2019;17(12):2356–68.
30. Nagarajan S, Hossan T, Alawi M, Najafova Z, Indenbirken D, Bedi U, et al. Bromodomain protein BRD4 is required for estrogen receptor-dependent enhancer activation and gene transcription. Cell Rep. 2014;8(2):460–9.
31. Garcia-Carpizo V, Ruiz-Llorente S, Sarmentero J, Gonzalez-Corpas A, Barrero MJ. CREBBP/EP300 Bromodomain Inhibition Affects the Proliferation of AR-Positive Breast Cancer Cell Lines. Mol Cancer Res. 2019;17(3):720–30.
32. Xu L, Chen Y, Mayakonda A, Koh L, Chong YK, Buckley DL, et al. Targetable BET proteins- and E2F1-dependent transcriptional program maintains the malignancy of glioblastoma. Proc Natl Acad Sci U S A. 2018;115(22):E5086–E95.
33. Stokes ME, Vasciaveo A, Small JC, Zask A, Reznik E, Smith N, et al. Subtype-selective prenylated isoflavonoids disrupt regulatory drivers of MYCN-amplified cancers. Cell Chem Biol. 2024;31(4):805–19 e9.
34. Cancer M, Drews LF, Bengtsson J, Bolin S, Rosen G, Westermark B, et al. BET and Aurora Kinase A inhibitors synergize against MYCN-positive human glioblastoma cells. Cell Death Dis. 2019;10(12):881.
35. Li M, Han Y, Wang C, Kang W, Jiang W, Zhang L, et al. Dissecting super-enhancer driven transcriptional dependencies reveals novel therapeutic strategies and targets for group 3 subtype medulloblastoma. J Exp Clin Cancer Res. 2022;41(1):311.
36. Iniguez AB, Alexe G, Wang EJ, Roti G, Patel S, Chen L, et al. Resistance to Epigenetic-Targeted Therapy Engenders Tumor Cell Vulnerabilities Associated with Enhancer Remodeling. Cancer Cell. 2018;34(6):922–38 e7.

37. Gao Y, Volegova M, Nasholm N, Das S, Kwiatkowski N, Abraham BJ, et al. Synergistic Anti-Tumor Effect of Combining Selective CDK7 and BRD4 Inhibition in Neuroblastoma. Front Oncol. 2021;11:773186.
38. Echevarria-Vargas IM, Reyes-Uribe PI, Guterres AN, Yin X, Kossenkov AV, Liu Q, et al. Co-targeting BET and MEK as salvage therapy for MAPK and checkpoint inhibitor-resistant melanoma. EMBO Mol Med. 2018;10(5).
39. Fontanals-Cirera B, Hasson D, Vardabasso C, Di Micco R, Agrawal P, Chowdhury A, et al. Harnessing BET Inhibitor Sensitivity Reveals AMIGO2 as a Melanoma Survival Gene. Mol Cell. 2017;68(4):731–44 e9.
40. Dong J, Li J, Li Y, Ma Z, Yu Y, Wang CY. Transcriptional super-enhancers control cancer stemness and metastasis genes in squamous cell carcinoma. Nat Commun. 2021;12(1):3974.
41. Wu T, Wang G, Chen W, Zhu Z, Liu Y, Huang Z, et al. Co-inhibition of BET proteins and NF-kappaB as a potential therapy for colorectal cancer through synergistic inhibiting MYC and FOXM1 expressions. Cell Death Dis. 2018;9(3):315.
42. Wagner S, Vlachogiannis G, De Haven Brandon A, Valenti M, Box G, Jenkins L, et al. Suppression of interferon gene expression overcomes resistance to MEK inhibition in KRAS-mutant colorectal cancer. Oncogene. 2019;38(10):1717–33.
43. Principe DR, Xiong R, Li Y, Pham TND, Kamath SD, Dubrovskyi O, et al. XP-524 is a dual-BET/EP300 inhibitor that represses oncogenic KRAS and potentiates immune checkpoint inhibition in pancreatic cancer. Proc Natl Acad Sci U S A. 2022;119(4).
44. Hemming ML, Lawlor MA, Andersen JL, Hagan T, Chipashvili O, Scott TG, et al. Enhancer Domains in Gastrointestinal Stromal Tumor Regulate KIT Expression and Are Targetable by BET Bromodomain Inhibition. Cancer Res. 2019;79(5):994–1009.
45. Li F, Liu P, Mi W, Li L, Anderson NM, Lesner NP, et al. Blocking methionine catabolism induces senescence and confers vulnerability to GSK3 inhibition in liver cancer. Nat Cancer. 2024;5(1):131–46.
46. Baek M, Chai JC, Choi HI, Yoo E, Binas B, Lee YS, et al. Comprehensive transcriptome profiling of BET inhibitor-treated HepG2 cells. PLoS One. 2022;17(4):e0266966.
47. McCleland ML, Mesh K, Lorenzana E, Chopra VS, Segal E, Watanabe C, et al. CCAT1 is an enhancer-templated RNA that predicts BET sensitivity in colorectal cancer. J Clin Invest. 2016;126(2):639–52.
48. Zhu Y, Lee H, White S, Weimer AK, Monte E, Horning A, et al. Global loss of promoter-enhancer connectivity and rebalancing of gene expression during early colorectal cancer carcinogenesis. Nat Cancer. 2024;5(11):1697–712.
49. Chen H, Gesumaria L, Park YK, Oliver TG, Singer DS, Ge K, et al. BET Inhibitors Target the SCLC-N Subtype of Small-Cell Lung Cancer by Blocking NEUROD1 Transactivation. Mol Cancer Res. 2023;21(2):91–101.
50. Zhong M, Li X, Zhao F, Huang Y, Long Y, Chen K, et al. Natural compound library screening identifies Sanguinarine chloride for the treatment of SCLC by upregulating CDKN1A. Transl Oncol. 2022;17:101345.
51. Szczepanski A, Tsuboyama N, Lyu H, Wang P, Beytullahoglu O, Zhang T, et al. A SWI/SNF-dependent transcriptional regulation mediated by POU2AF2/C11orf53 at enhancer. Nat Commun. 2024;15(1):2067.
52. Handoko L, Kaczkowski B, Hon CC, Lizio M, Wakamori M, Matsuda T, et al. JQ1 affects BRD2-dependent and independent transcription regulation without disrupting H4-hyperacetylated chromatin states. Epigenetics. 2018;13(4):410–31.
53. Boedicker C, Hussong M, Grimm C, Dolgikh N, Meister MT, Enssle JC, et al. Co-inhibition of BET proteins and PI3Kalpha triggers mitochondrial apoptosis in rhabdomyosarcoma cells. Oncogene. 2020;39(19):3837–52.
54. Ishi Y, Zhang Y, Zhang A, Sasaki T, Piunti A, Suri A, et al. Therapeutic Targeting of EZH2 and BET BRD4 in Pediatric Rhabdoid Tumors. Mol Cancer Ther. 2022;21(5):715–26.

913 55. Gollavilli PN, Pawar A, Wilder-Romans K, Natesan R, Engelke CG, Dommeti VL, et al.
914 EWS/ETS-Driven Ewing Sarcoma Requires BET Bromodomain Proteins. Cancer Res.
915 2018;78(16):4760–73.
916 56. Kurimchak AM, Shelton C, Duncan KE, Johnson KJ, Brown J, O'Brien S, et al.
917 Resistance to BET Bromodomain Inhibitors Is Mediated by Kinome Reprogramming in Ovarian
918 Cancer. Cell Rep. 2016;16(5):1273–86.
919 57. Zheng J, Huang B, Xiao L, Wu M. Effects of BRD4 inhibitor JQ1 on the expression
920 profile of super-enhancer related lncRNAs and mRNAs in cervical cancer HeLa cells. PeerJ.
921 2024;12:e17035.
922 58. Oh DH, Ma X, Hogg SJ, He J, Kearney C, Brasacchio D, et al. Rationally designed
923 chimeric PI3K-BET bromodomain inhibitors elicit curative responses in MYC-driven lymphoma.
924 Proc Natl Acad Sci U S A. 2023;120(36):e2306414120.
925 59. Winter GE, Mayer A, Buckley DL, Erb MA, Roderick JE, Vittori S, et al. BET
926 Bromodomain Proteins Function as Master Transcription Elongation Factors Independent of
927 CDK9 Recruitment. Mol Cell. 2017;67(1):5–18 e9.
928 60. Garcia-Carpizo V, Ruiz-Llorente S, Sarmentero J, Grana-Castro O, Pisano DG, Barrero
929 MJ. CREBBP/EP300 bromodomains are critical to sustain the GATA1/MYC regulatory axis in
930 proliferation. Epigenetics Chromatin. 2018;11(1):30.
931 61. Ott CJ, Federation AJ, Schwartz LS, Kasar S, Klitgaard JL, Lenci R, et al. Enhancer
932 Architecture and Essential Core Regulatory Circuitry of Chronic Lymphocytic Leukemia. Cancer
933 Cell. 2018;34(6):982–95 e7.
934 62. Jin Q, Martinez CA, Arcipowski KM, Zhu Y, Gutierrez-Diaz BT, Wang KK, et al. USP7
935 Cooperates with NOTCH1 to Drive the Oncogenic Transcriptional Program in T-Cell Leukemia.
936 Clin Cancer Res. 2019;25(1):222–39.
937 63. Decker TM, Kluge M, Krebs S, Shah N, Blum H, Friedel CC, et al. Transcriptome
938 analysis of dominant-negative Brd4 mutants identifies Brd4-specific target genes of small
939 molecule inhibitor JQ1. Sci Rep. 2017;7(1):1684.
940 64. McCalmont H, Li KL, Jones L, Toubia J, Bray SC, Casolari DA, et al. Efficacy of
941 combined CDK9/BET inhibition in preclinical models of MLL-rearranged acute leukemia. Blood
942 Adv. 2020;4(2):296–300.
943 65. Lee E, Archasappawat S, Ji K, Pena J, Fernandez-Vega V, Gangaraju R, et al. A new
944 vulnerability to BET inhibition due to enhanced autophagy in BRCA2 deficient pancreatic
945 cancer. Cell Death Dis. 2023;14(9):620.
946 66. Das D, Leung JY, Balamurugan S, Tergaonkar V, Loh AHP, Chiang CM, et al. BRD4
947 isoforms have distinct roles in tumour progression and metastasis in rhabdomyosarcoma.
948 EMBO Rep. 2024;25(2):832–52.
949 67. Hussong M, Borno ST, Kerick M, Wunderlich A, Franz A, Sultmann H, et al. The
950 bromodomain protein BRD4 regulates the KEAP1/NRF2-dependent oxidative stress response.
951 Cell Death Dis. 2014;5(4):e1195.
952 68. Liu L, Lin B, Yin S, Ball LE, Delaney JR, Long DT, et al. Arginine methylation of BRD4 by
953 PRMT2/4 governs transcription and DNA repair. Sci Adv. 2022;8(49):eadd8928.
954 69. Sakamaki JI, Wilkinson S, Hahn M, Tasdemir N, O'Prey J, Clark W, et al. Bromodomain
955 Protein BRD4 Is a Transcriptional Repressor of Autophagy and Lysosomal Function. Mol Cell.
956 2017;66(4):517–32 e9.
957 70. Shu S, Wu HJ, Ge JY, Zeid R, Harris IS, Jovanovic B, et al. Synthetic Lethal and
958 Resistance Interactions with BET Bromodomain Inhibitors in Triple-Negative Breast Cancer. Mol
959 Cell. 2020;78(6):1096–113 e8.
960 71. Ito T, Young MJ, Li R, Jain S, Wernitznig A, Krill-Burger JM, et al. Paralog knockout
961 profiling identifies DUSP4 and DUSP6 as a digenic dependence in MAPK pathway-driven
962 cancers. Nat Genet. 2021;53(12):1664–72.

963 72. Shinohara H, Sawado R, Nakagawa M, Hattori A, Yamagata K, Tauchi K, et al. Dual
964 targeting of EZH1 and EZH2 for the treatment of malignant rhabdoid tumors. Mol Ther
965 Oncolytics. 2022;27:14–25.
966 73. Patel PO, Pishas KI, Taslim C, Selich-Anderson J, Theisen ER, Lessnick SL.
967 Investigating the role of LSD2 as an epigenetic regulator in Ewing sarcoma. Oncotarget.
968 2019;10(39):3865–78.
969 74. Hsu SC, Gilgenast TG, Bartman CR, Edwards CR, Stonestrom AJ, Huang P, et al. The
970 BET Protein BRD2 Cooperates with CTCF to Enforce Transcriptional and Architectural
971 Boundaries. Mol Cell. 2017;66(1):102–16 e7.
972 75. Xie L, Dong P, Qi Y, Hsieh TS, English BP, Jung S, et al. BRD2 compartmentalizes the
973 accessible genome. Nat Genet. 2022;54(4):481–91.
974 76. Saenz DT, Fiskus W, Qian Y, Manshouri T, Rajapakshe K, Raina K, et al. Novel BET
975 protein proteolysis-targeting chimera exerts superior lethal activity than bromodomain inhibitor
976 (BETi) against post-myeloproliferative neoplasm secondary (s) AML cells. Leukemia.
977 2017;31(9):1951–61.

978

Fig. 1 **Pan-cancer BRD2 upregulation upon BET inhibition.**

A **Pan-cancer *BRD2* expression in response to JQ1**

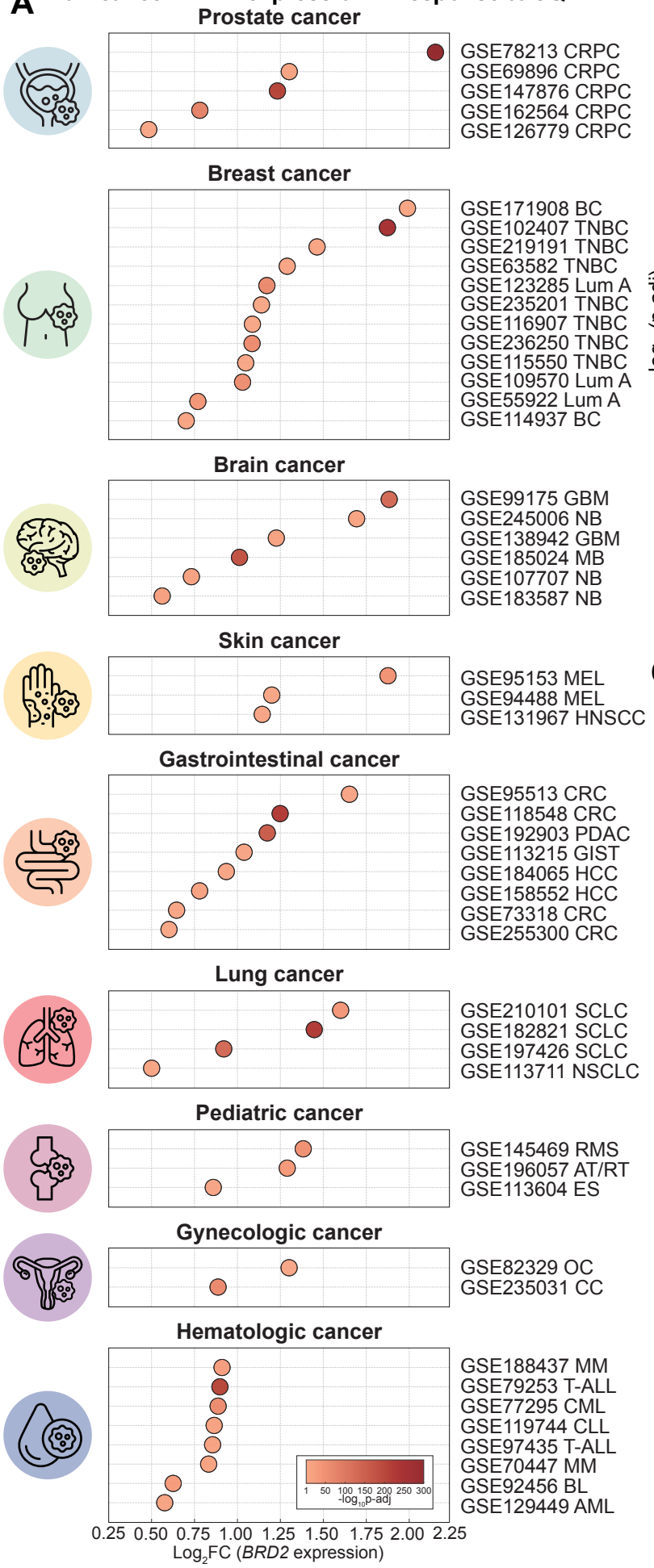

B **GSE78213**

Differentially expressed genes

JQ1 vs. DMSO in castration resistant prostate cancer

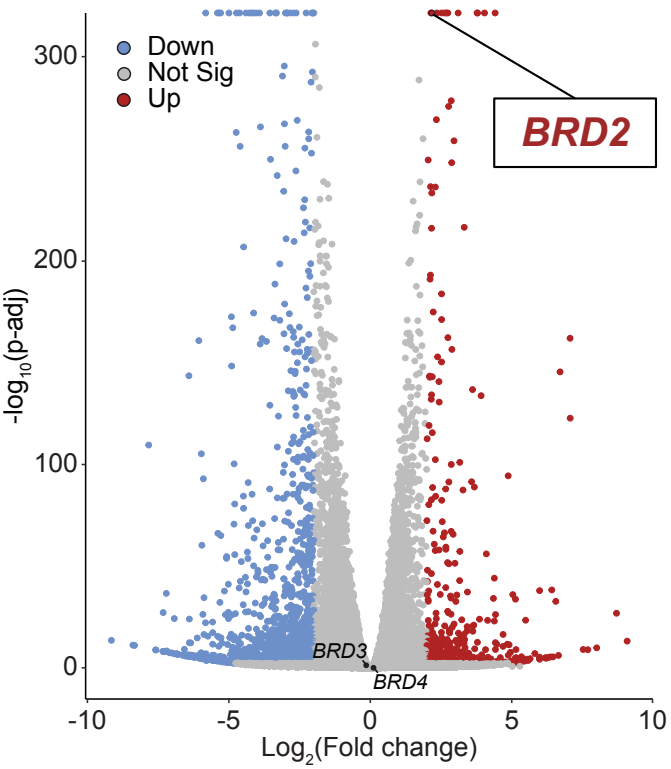

C

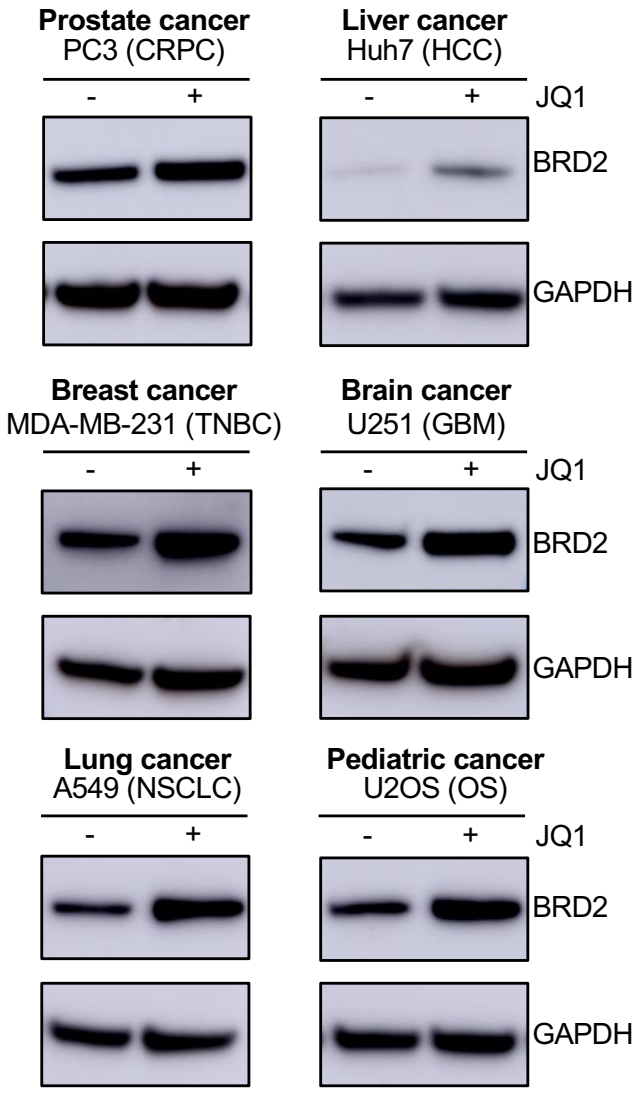

Fig. 2 **Pharmacological BET inhibition uniquely drives BRD2 upregulation in pancreatic cancer.**

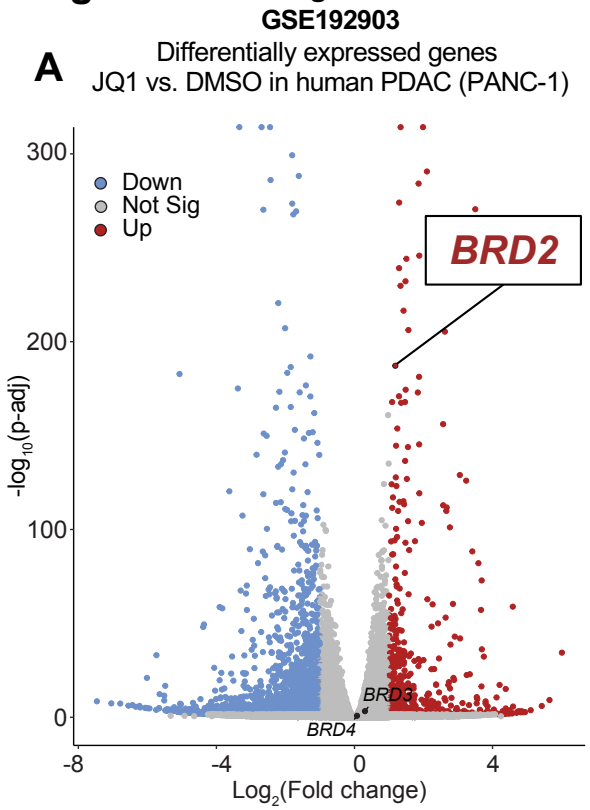

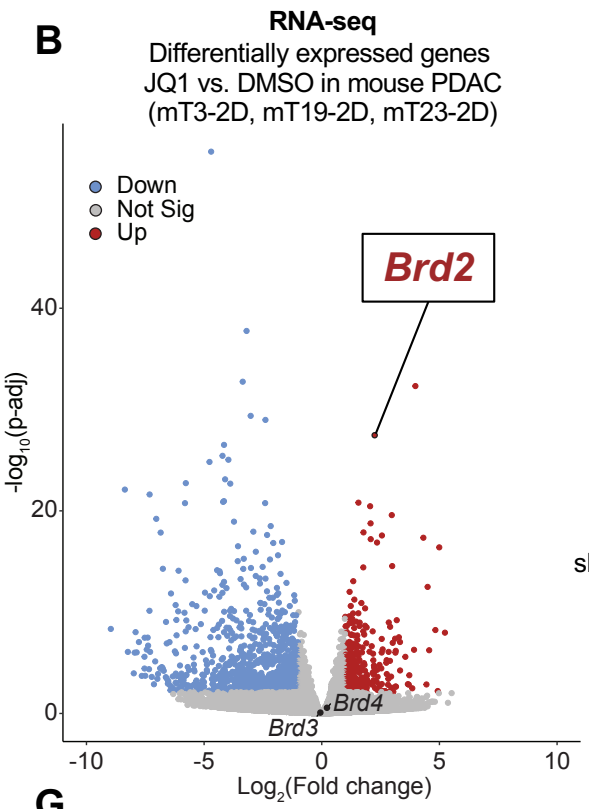

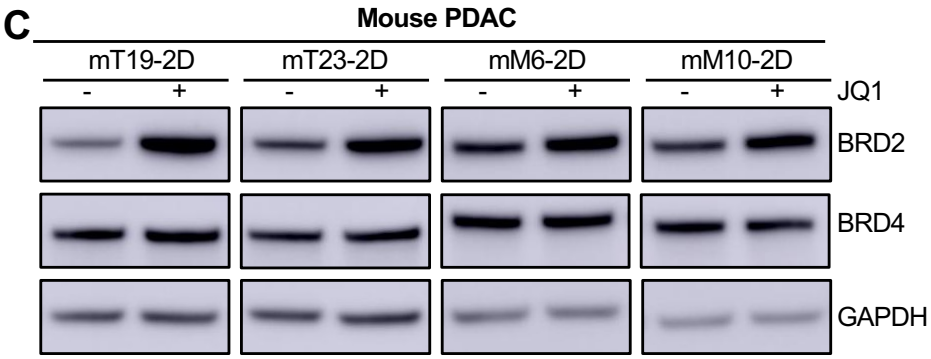

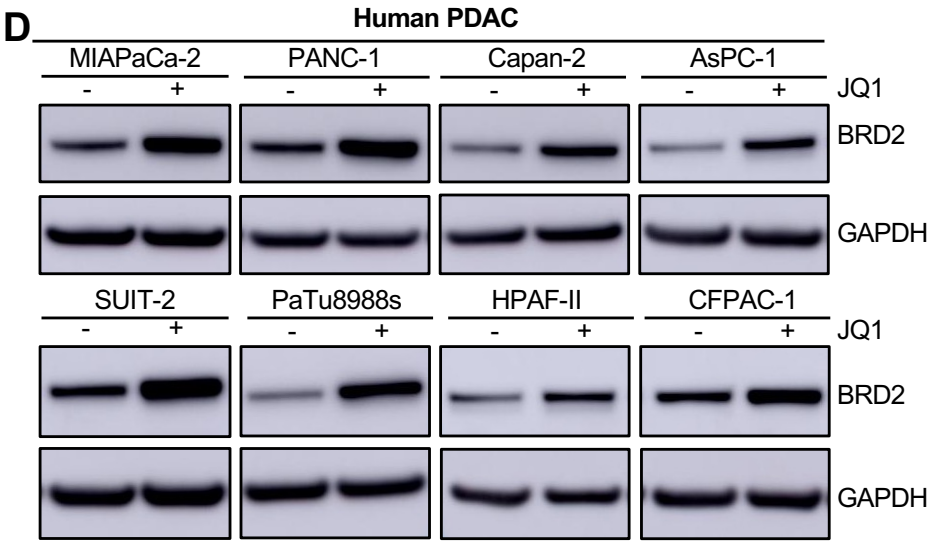

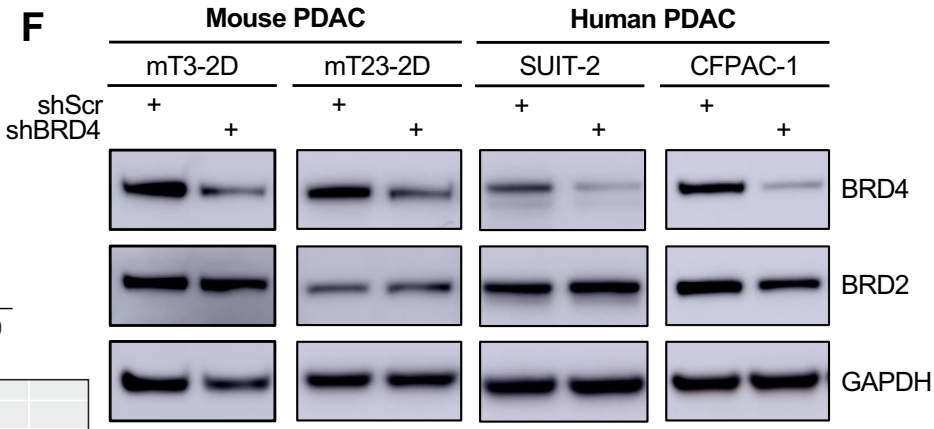

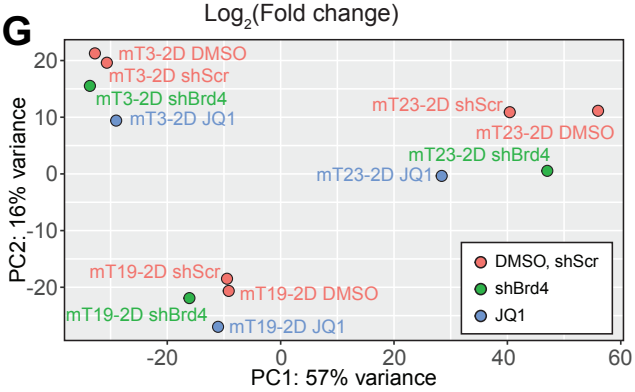

Fig. 3 **NFYA as a candidate transcriptional regulator of BRD2 induction upon BET inhibition.**

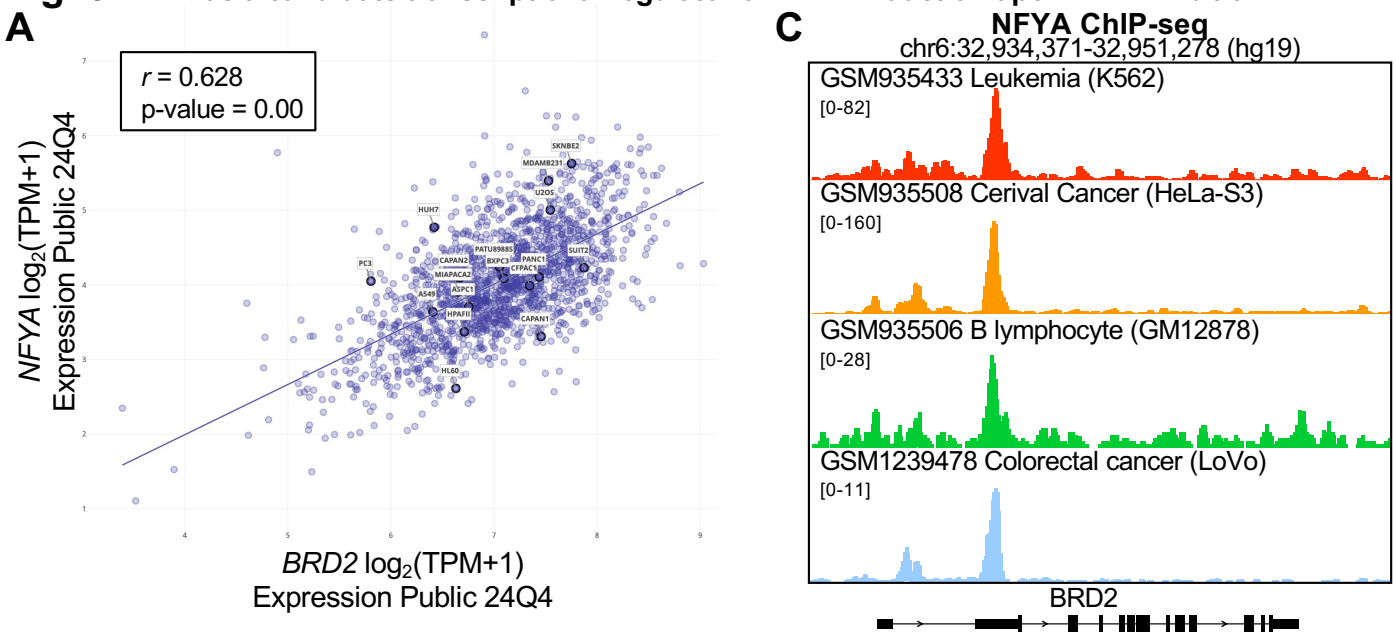

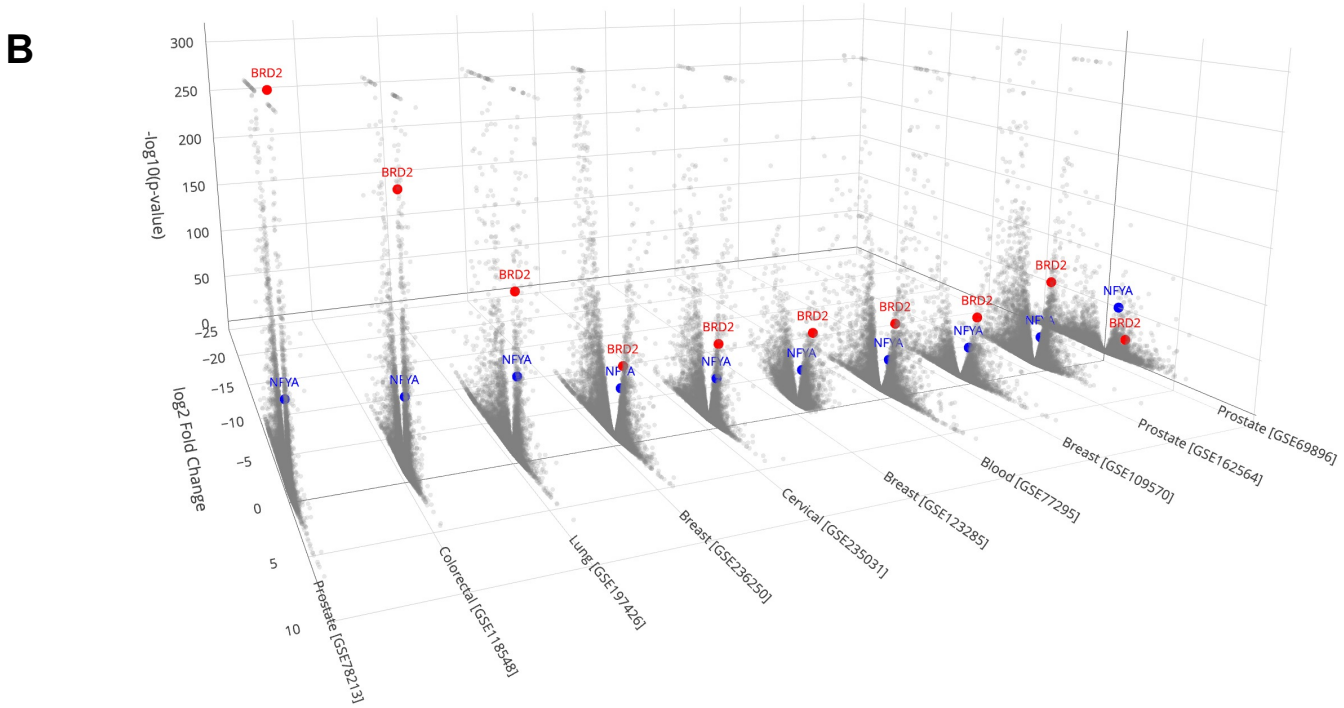

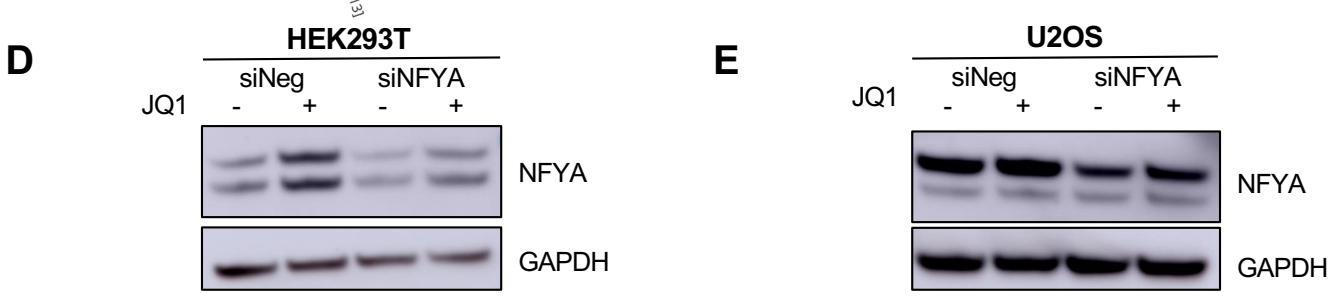

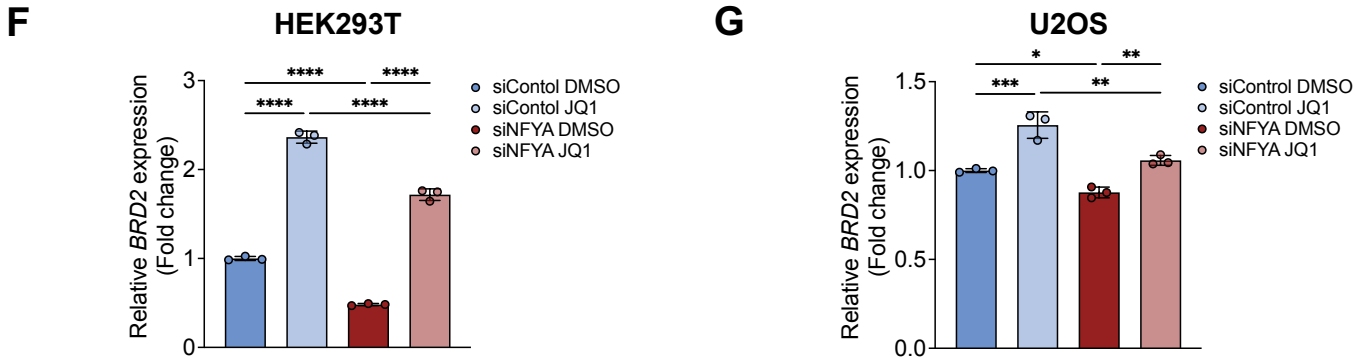

Fig. 4 **BRD2 depletion sensitizes cancer cells to BET inhibition.**

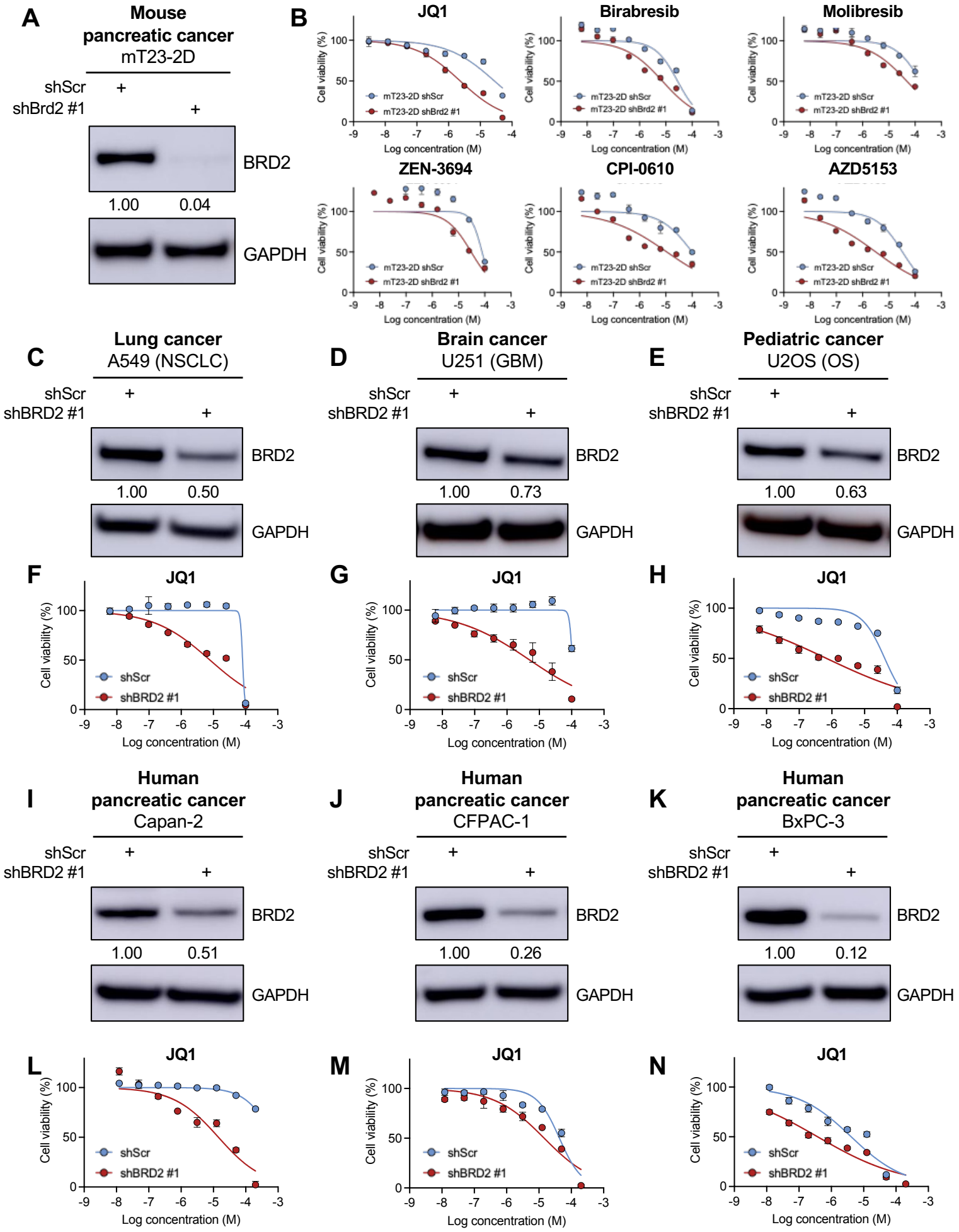

Fig. 5 Genetic BRD2 perturbation enhances the antitumor effect of BET inhibition *in vivo*.

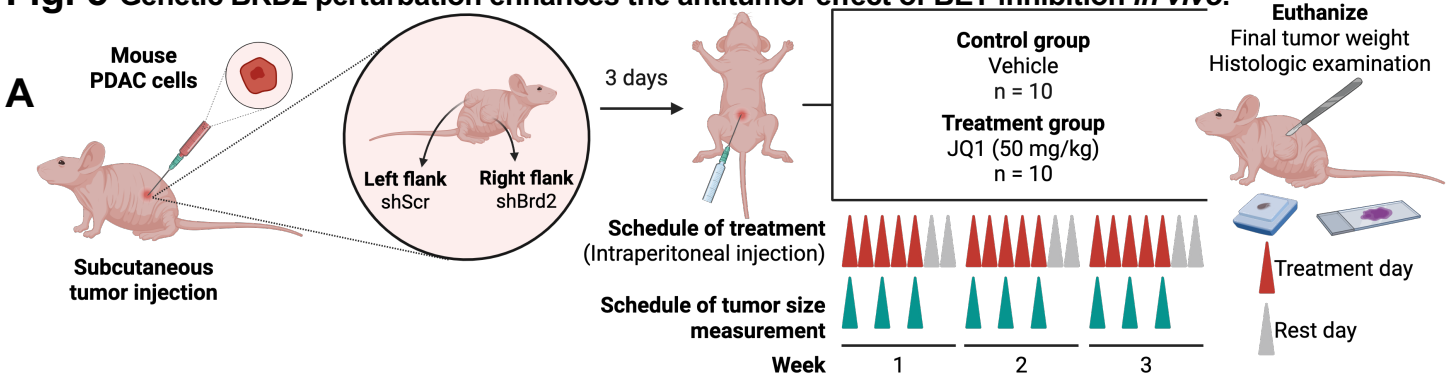

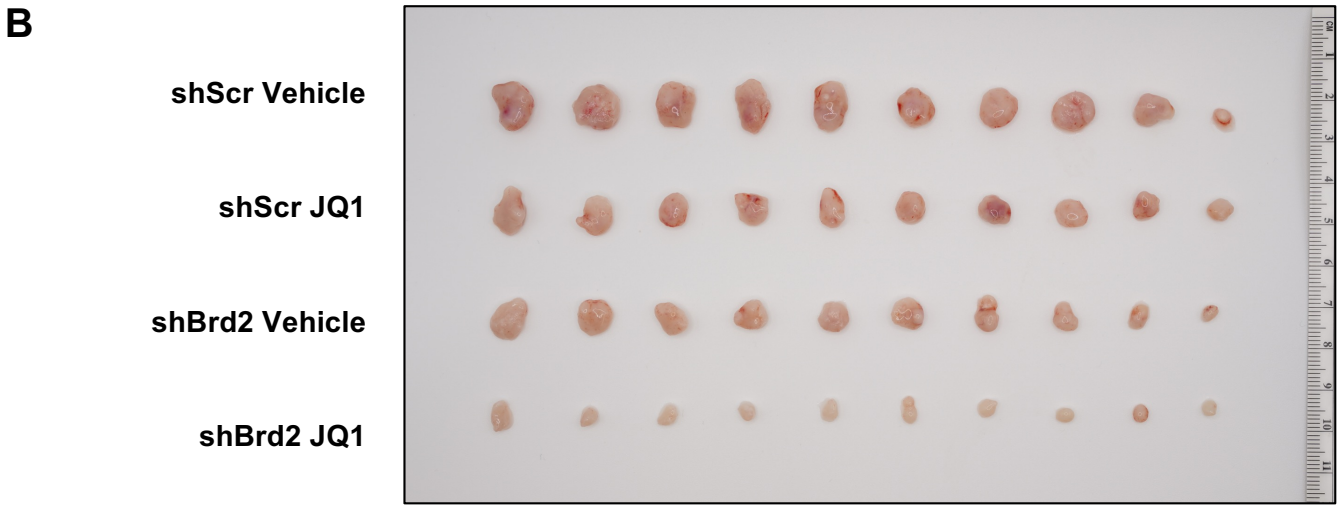

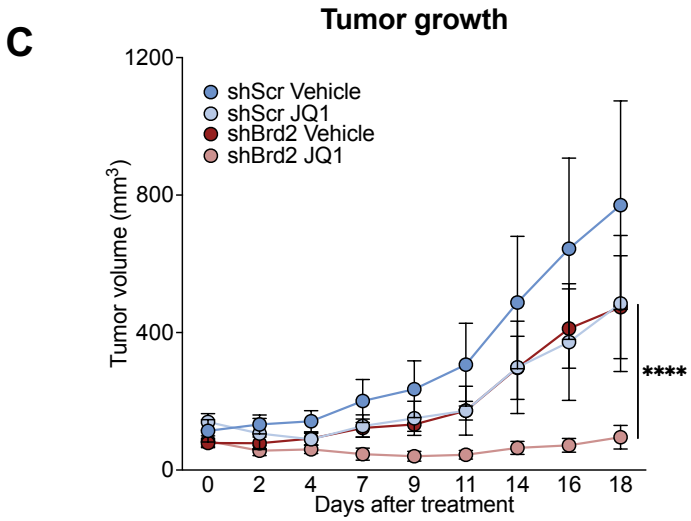

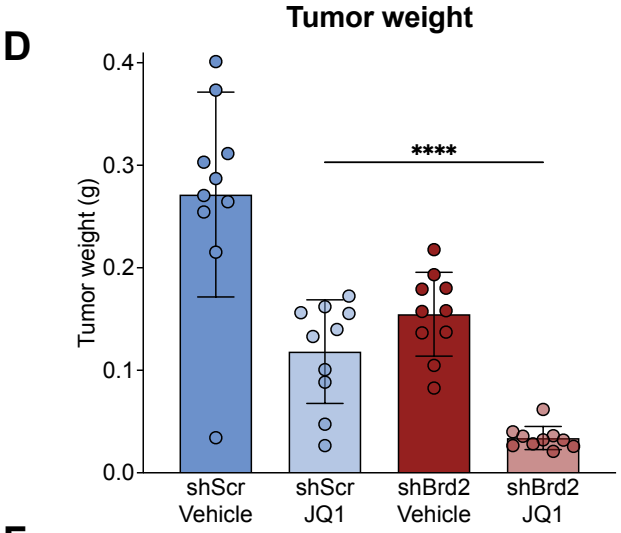

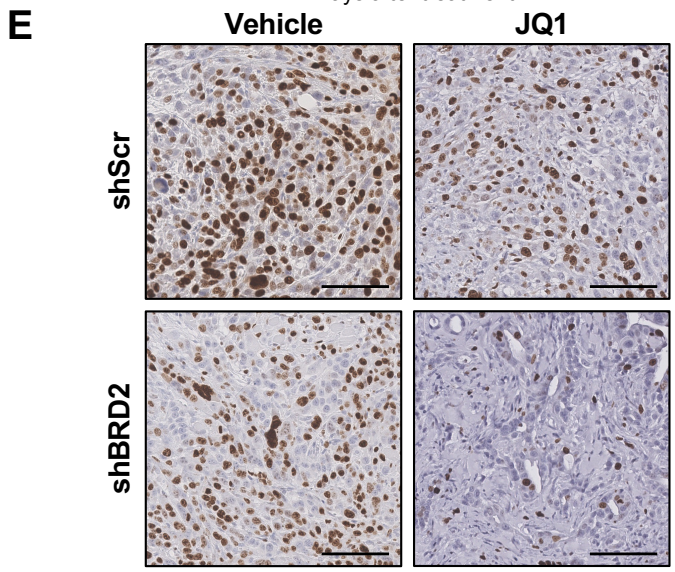

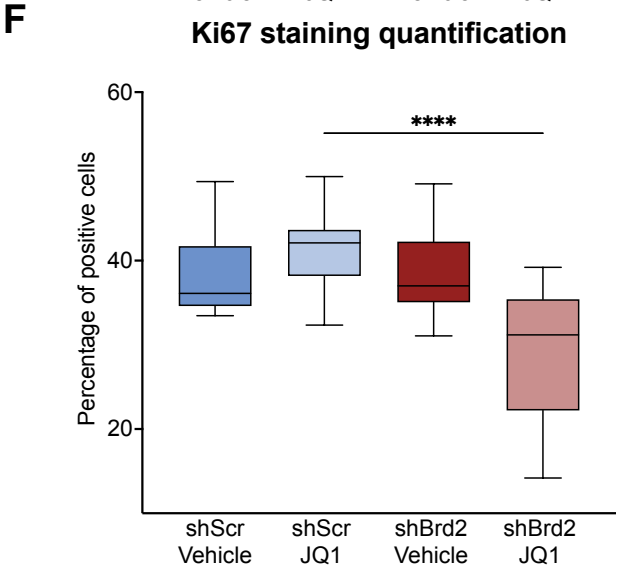

Fig. 6 **BRD2 retention sustains transcriptional programs in BETi-resistant pancreatic cancer cells.**

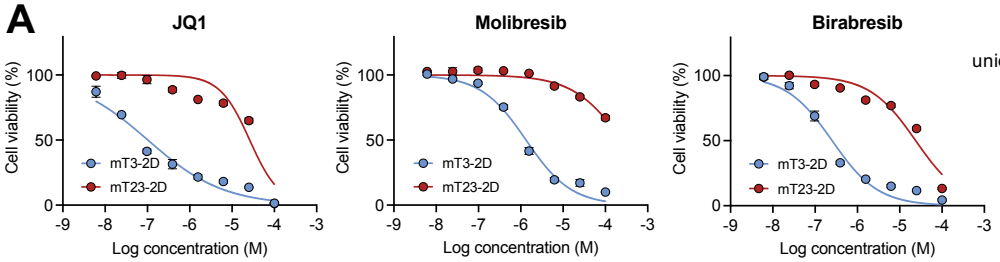

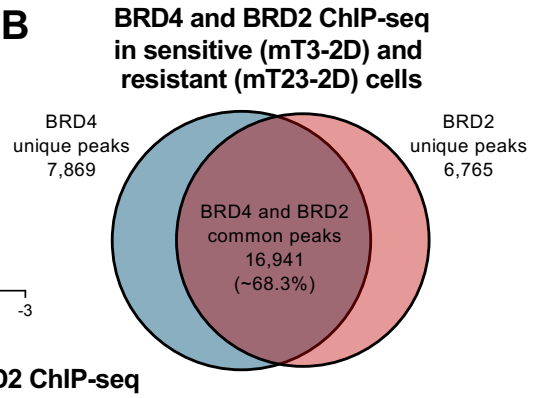

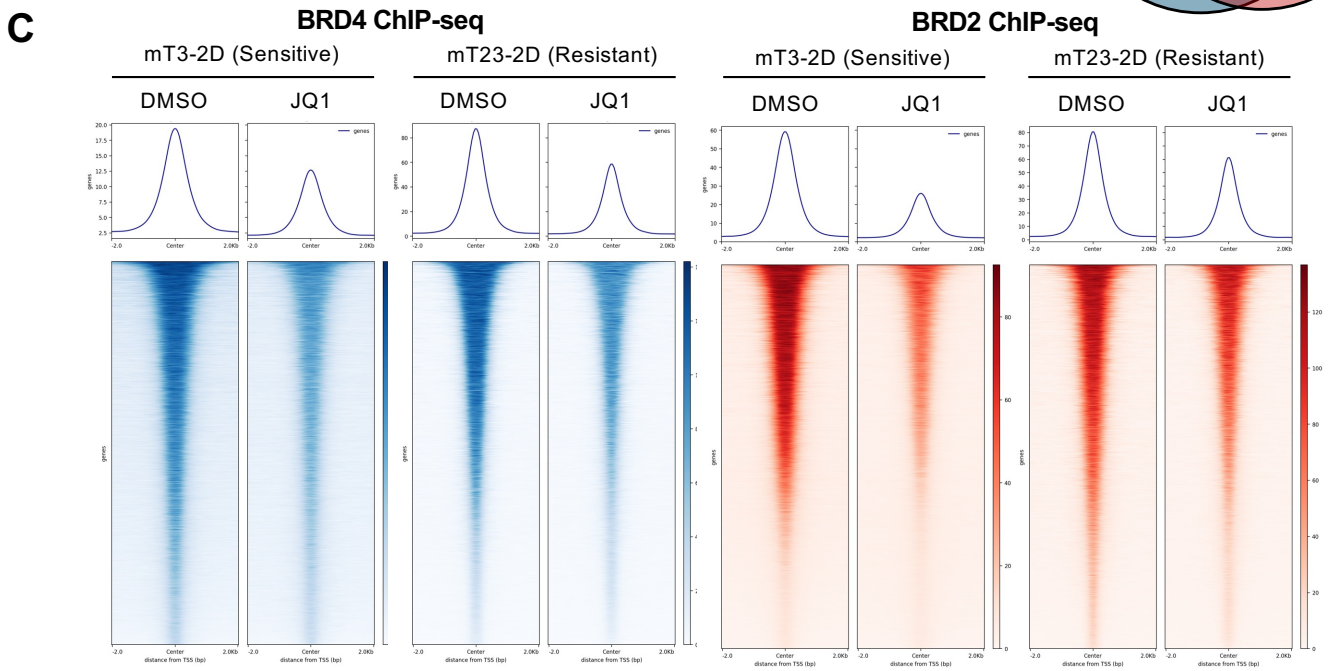

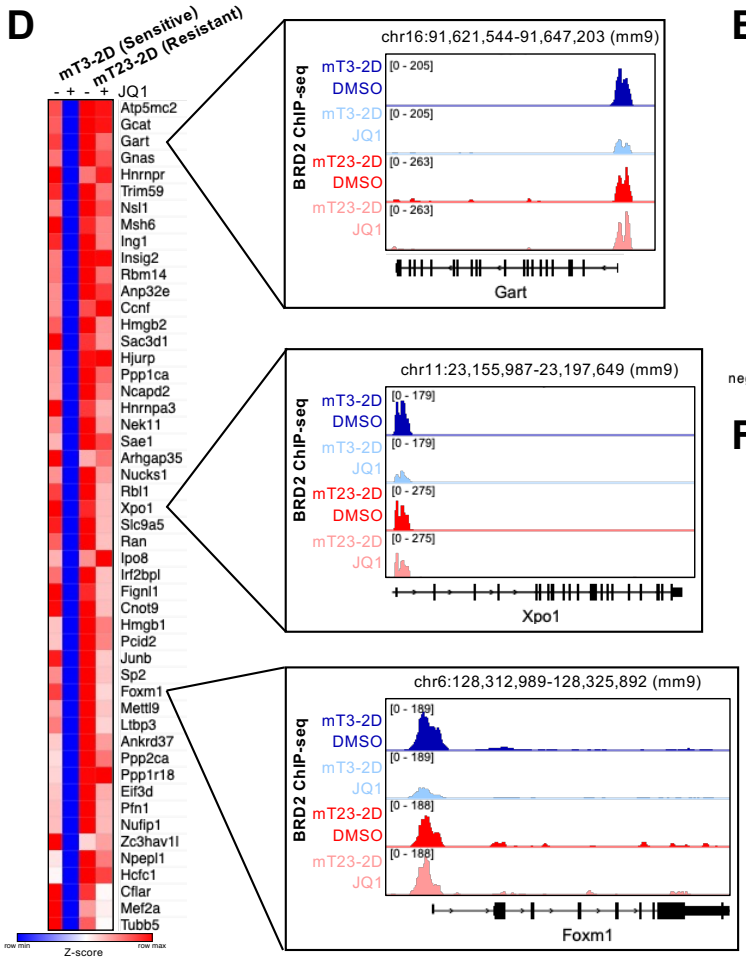

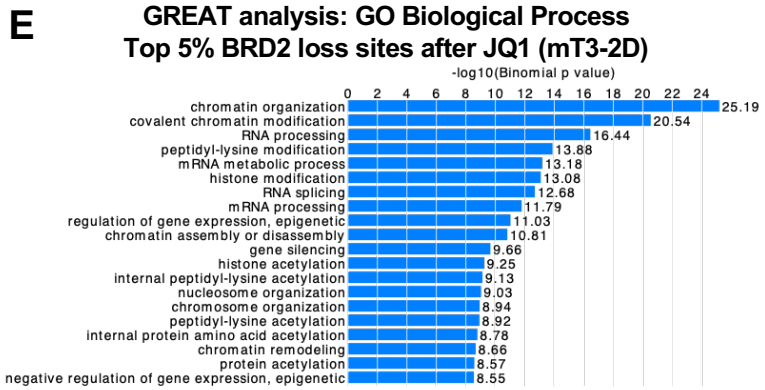

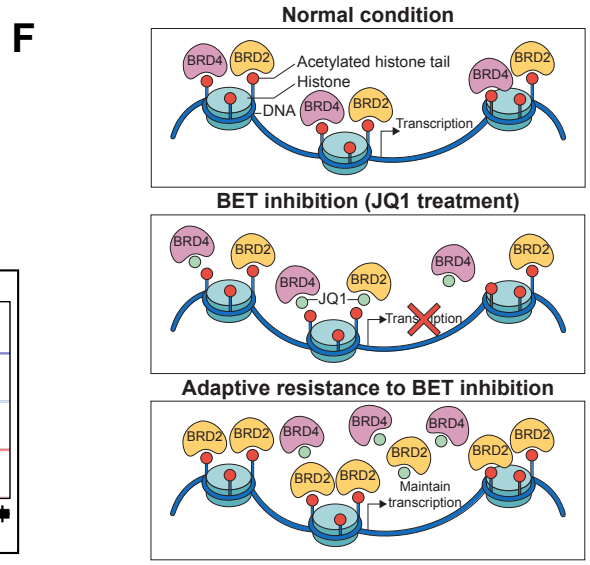

Supplementary Fig. 1

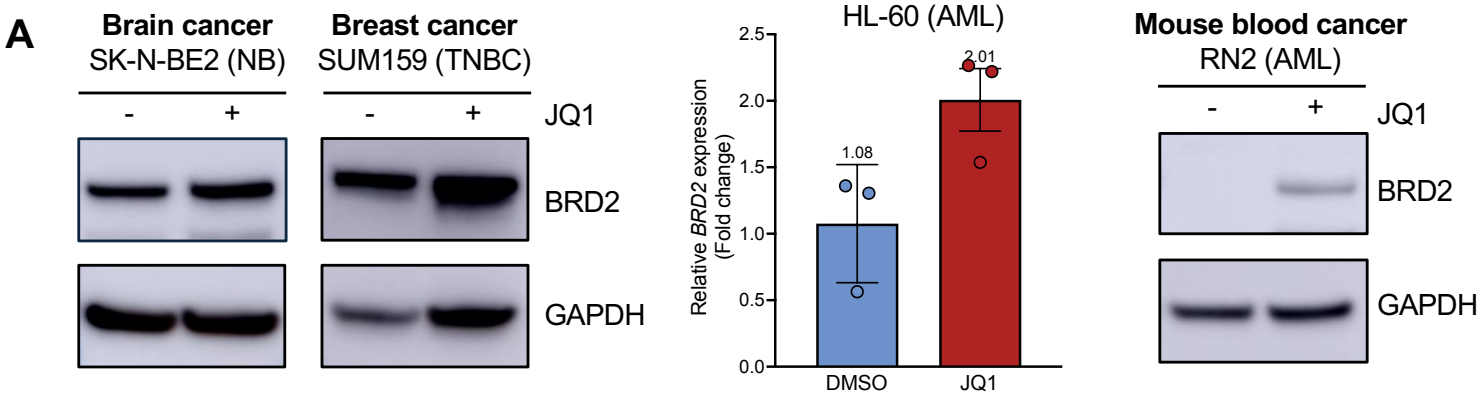

Supplementary Fig. 2

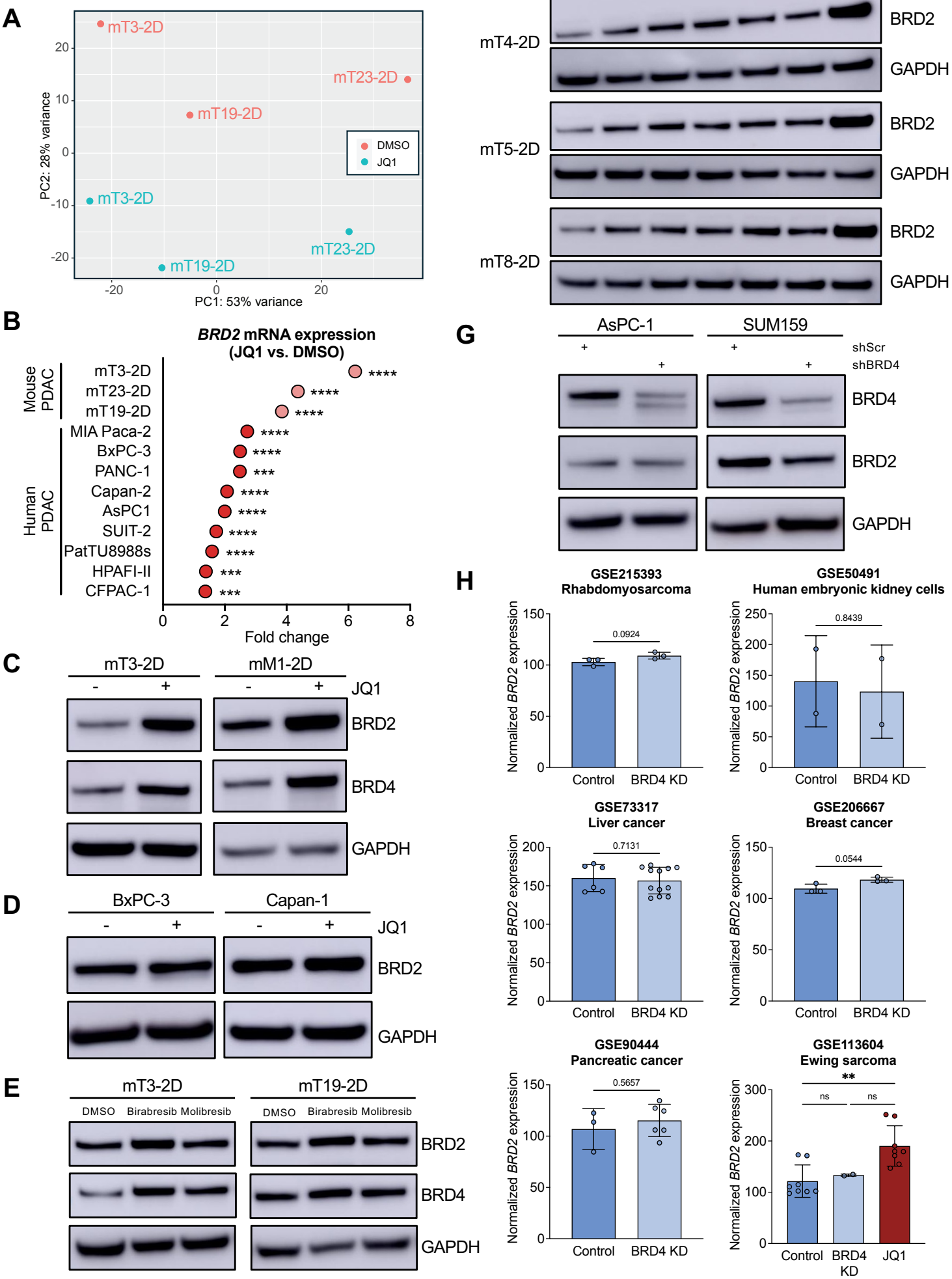

Supplementary Fig. 3

A

	Gene	Function	hsa-u.4 / BRD2	hsa-r.6 / BRD2	hsa-m.7 / BRD2	hsa-m2.4 / BRD2
1	PPP1R10	protein phosphatase 1 regulatory subunit 10	8.9	8.1	5	7.7
2	NXF1	nuclear RNA export factor 1	8	6.9	2.9	7.1
3	POLR2A	RNA polymerase II subunit A	7.6	6.7	2.8	6.6
4	RBM22	RNA binding motif protein 22	7.5	7.8	2.6	5.3
5	FAM193A	family with sequence similarity 193 member A	7.4	7.4	1.1	5.6
6	BRPF3	bromodomain and PHD finger containing 3	7.1	5.5	1.7	6.9
7	PRRC2A	proline rich coiled-coil 2A	6.8	6.2	3.4	5.8
8	BTN2A1	butyrophilin subfamily 2 member A1	6.8	6.7	1.9	5.1
9	TRIM39	tripartite motif containing 39	6.7	5.9	2.8	5.9
10	SRCAP	Snf2 related CREBBP activator protein	6.6	5	1.8	6.6
11	BRPF1	bromodomain and PHD finger containing 1	6.6	6.1	1.9	5.4
12	RSRC2	arginine and serine rich coiled-coil 2	6.6	7.1	2.9	4.4
13	KDM2A	lysine demethylase 2A	6.5	6.5	2.7	4.9
14	SCAF4	SR-related CTD associated factor 4	6.2	5.8	1	5.1
15	FAM53C	family with sequence similarity 53 member C	6.2	5.4	2.1	5.6
16	CCNL1	cyclin L1	6.2	6.8	1.3	4.1
17	EP300	E1A binding protein p300	6.2	5.4	1.9	5.5
18	ABCF1	ATP binding cassette subfamily F member 1	6.2	6	2.2	4.8
19	PHF12	PHD finger protein 12	6.1	5.8	1.2	5
20	CNOT4	CCR4-NOT transcription complex subunit 4	6.1	7.5	1.5	3.2
21	TRIM26	tripartite motif containing 26	6.1	7	2.6	3.7
22	ZNF592	zinc finger protein 592	6	4.1	0.6	6.4
23	ATXN2L	ataxin 2 like	5.9	5.1	1.9	5.3
24	ZNF335	zinc finger protein 335	5.8	5.3	1.8	5
25	SETD5	SET domain containing 5	5.8	6	2.3	4.2
26	CDK12	cyclin dependent kinase 12	5.8	6	0.6	4.2
27	NUP153	nucleoporin 153	5.8	5.6	1.8	4.5
28	CREBBP	CREB binding protein	5.8	5.2	0.9	5
29	SRRM2	serine/arginine repetitive matrix 2	5.8	4	5.1	6.2
30	**NFYA**	**nuclear transcription factor Y subunit alpha**	**5.7**	**5.6**	**1.7**	**4.4**

B

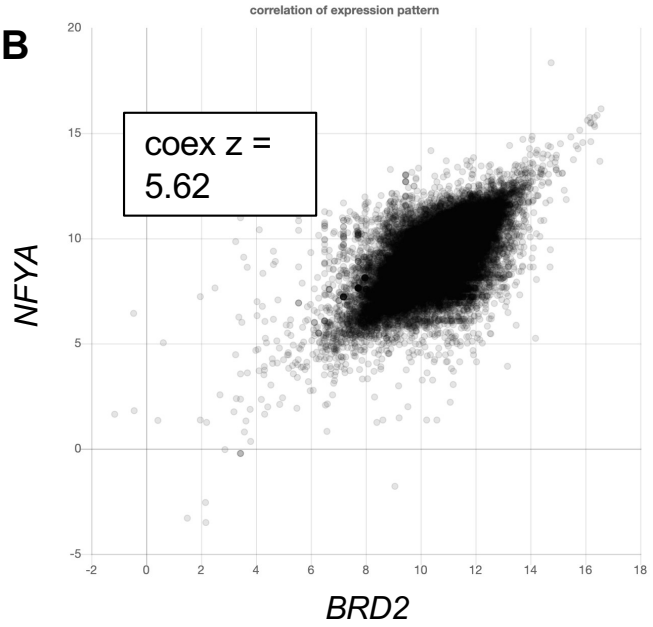

C

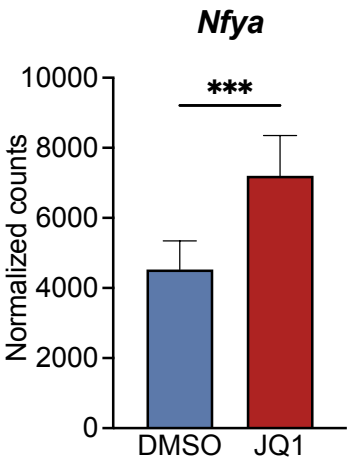

D

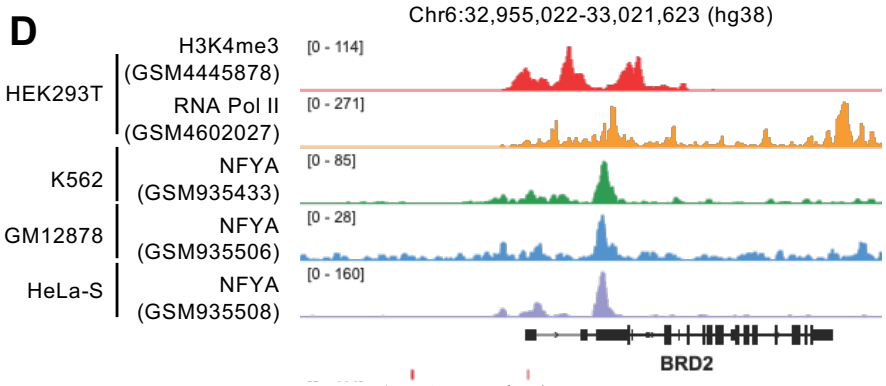

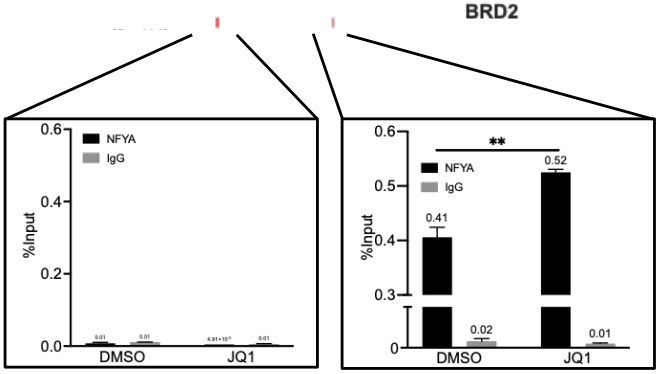

NFYA ChIP-qPCR

E

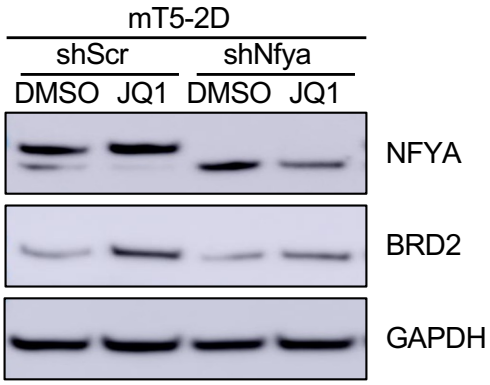

F

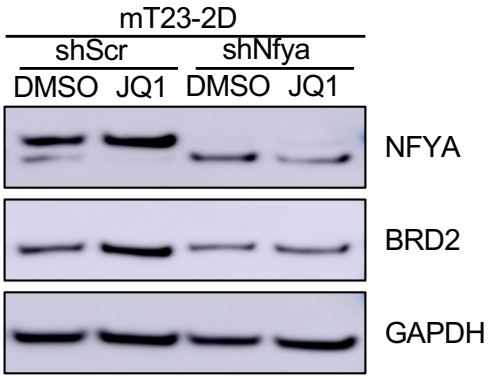

Supplementary Fig. 4

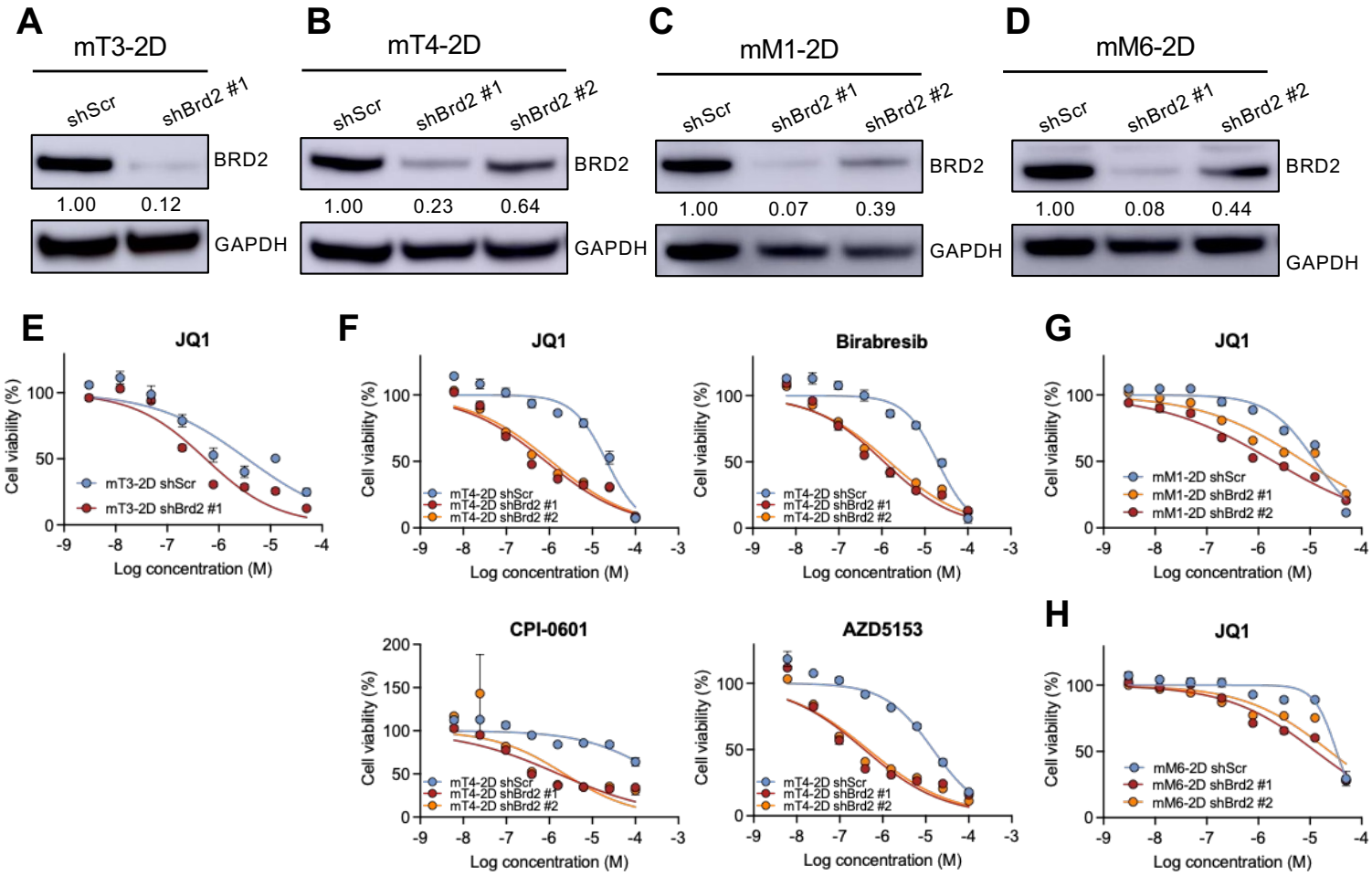

Supplementary Fig. 4

I

$LogIC_{50}$ and $\Delta LogIC_{50}$ of BETi sensitivity after BRD2 KD across cell lines

Drugs	Cell lines		$LogIC_{50}$ (M)	95% CI	$\Delta LogIC_{50}$
JQ1	mT23-2D	shScr	-4.556	-4.733 to -4.310	
		shBrd2 #1	-5.634	-5.760 to -5.506	1.078
	mT3-2D	shScr	-5.455	-5.769 to -5.104	
		shBrd2 #1	-6.258	-6.464 to -6.040	0.803
	mT4-2D	shScr	-4.667	-4.805 to -4.534	
		shBrd2 #1	-6.081	-6.291 to -5.864	1.414
		shBrd2 #2	-5.956	-6.128 to -5.782	1.289
	mM1-2D	shScr	-4.896	-5.018 to -4.776	
		shBrd2 #1	-5.704	-5.828 to -5.576	0.808
		shBrd2 #2	-5.112	-5.287 to -4.920	0.216
	mM6-2D	shScr	-4.486	-4.565 to -4.410	
		shBrd2 #1	-4.891	-5.047 to -4.718	0.405
		shBrd2 #2	-4.618	-4.844 to -4.305	0.132
	A549	shScr	-4.092	NE	
		shBRD2 #1	-5.105	-5.317 to -4.887	1.013
	U251	shScr	-3.979	NE	
		shBRD2 #1	-5.305	-5.576 to -5.022	1.326
	U2OS	shScr	-4.382	-4.538 to -4.249	
		shBRD2 #1	-6.163	-6.493 to -5.842	1.781
	Capan-2	shScr	-3.13	-3.314 to -2.871	
		shBRD2 #1	-4.845	-5.080 to -4.612	1.715
	CFPAC-1	shScr	-4.367	-4.514 to -4.233	
		shBRD2 #1	-4.839	-4.528 to -4.229	0.472
	BxPC-3	shScr	-5.386	-5.603 to -5.174	
		shBRD2 #1	-6.425	-6.638 to -6.224	1.039
Birabresib	mT23-2D	shScr	-4.551	-4.744 to -4.362	
		shBrd2 #1	-5.127	-5.316 to -4.933	0.576
	mT4-2D	shScr	-4.701	-4.845 to -4.561	
		shBrd2 #1	-5.949	-6.135 to -5.758	1.248
		shBrd2 #2	-5.825	-5.995 to -5.651	1.124
Molibresib	mT23-2D	shScr	-3.792	-4.045 to -3.236	
		shBrd2 #1	-4.311	-4.546 to -4.013	0.519
ZEN-3694	mT23-2D	shScr	-4.104	-4.401 to -3.686	
		shBrd2 #1	-4.52	-4.742 to -4.271	0.416
CPI-0610	mT23-2D	shScr	-4.003	-4.326 to -3.412	
		shBrd2 #1	-4.966	-5.265 to -4.619	0.963
	mT4-2D	shScr	-3.467	-3.872 to -2.656	
		shBrd2 #1	-5.651	-6.416 to -4.673	2.184
		shBrd2 #2	-5.787	-6.104 to -5.438	2.32
AZD5153	mT23-2D	shScr	-4.481	-4.708 to -4.229	
		shBrd2 #1	-5.497	-5.732 to -5.250	1.016
	mT4-2D	shScr	-4.832	-4.983 to -4.678	
		shBrd2 #1	-6.425	-6.709 to -6.124	1.593
		shBrd2 #2	-6.342	-6.539 to -6.141	1.51

IC_{50}: Half maximal inhibitory concentration
CI: Confidence interval
NE: Not estimable

Supplementary Fig. 4

J

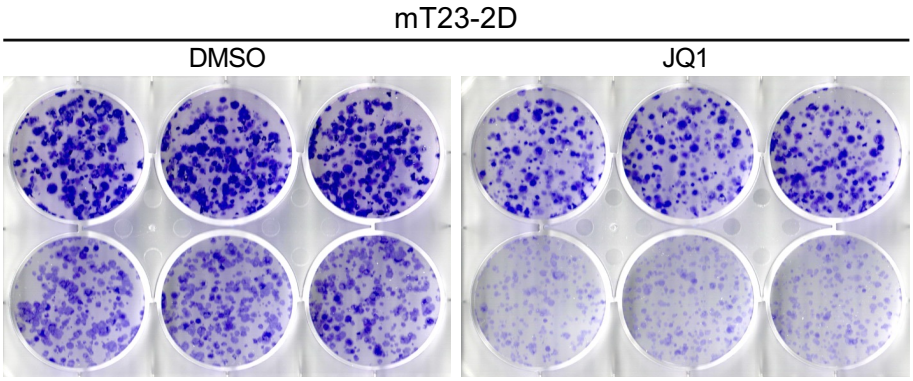

M

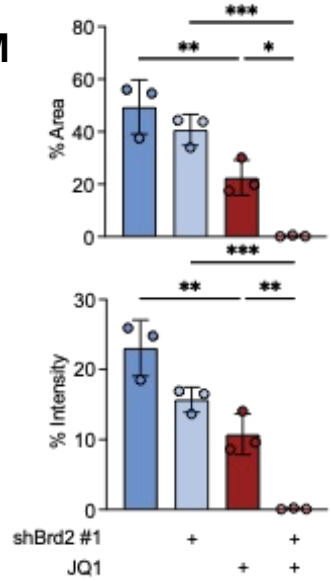

K

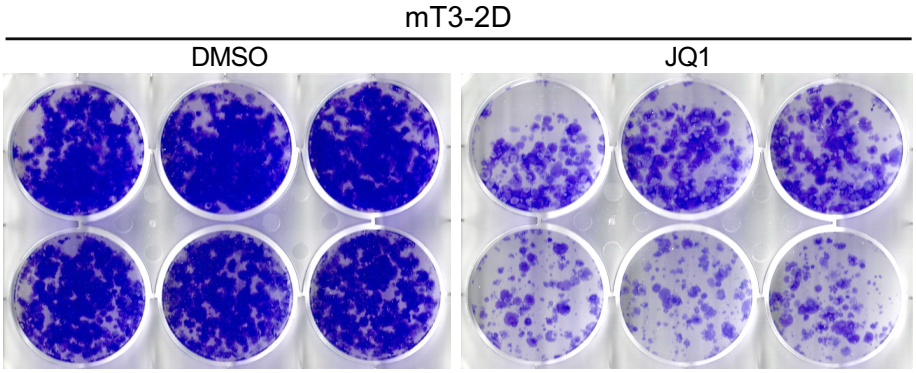

N

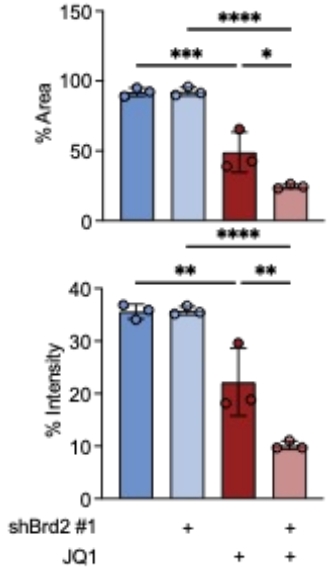

L

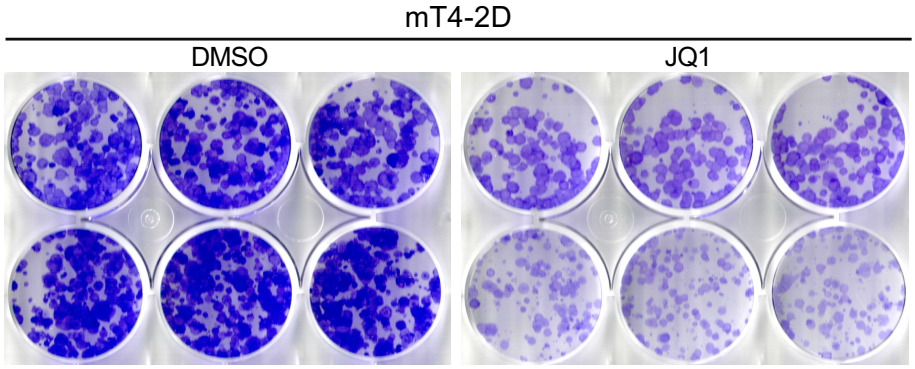

O

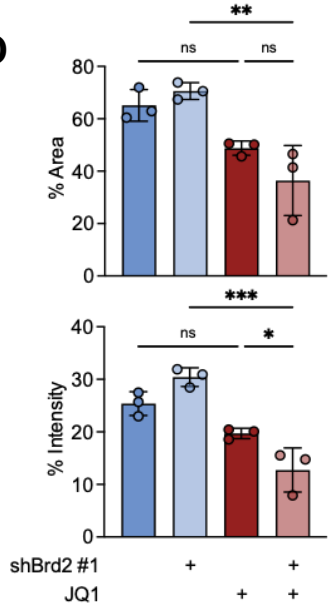

Supplementary Fig. 5

A

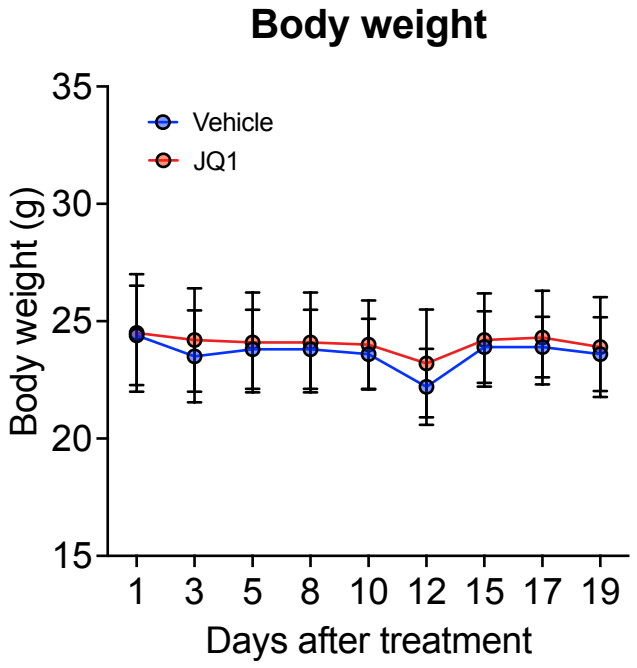

Supplementary Fig. 6

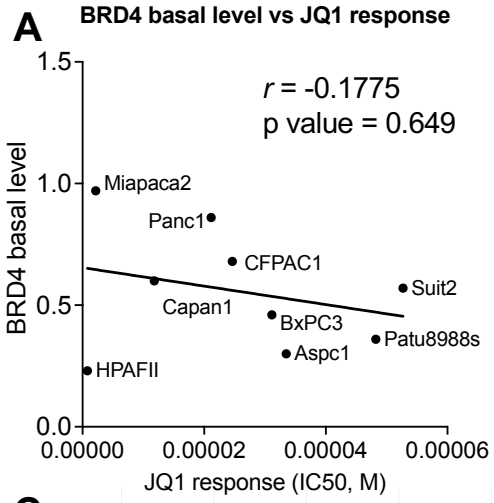

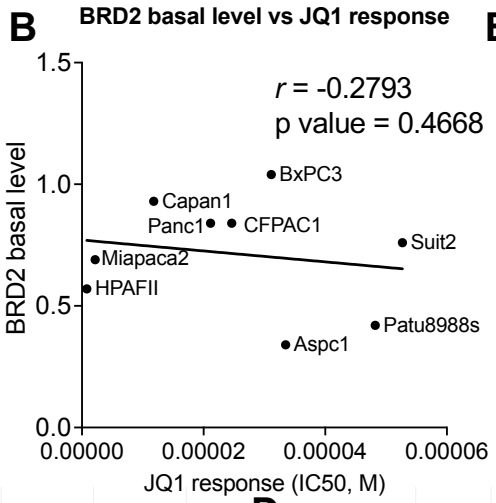

E
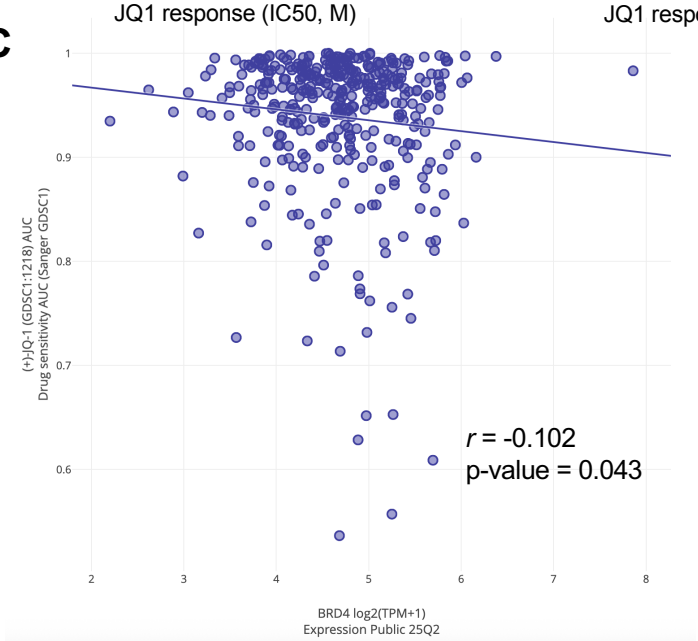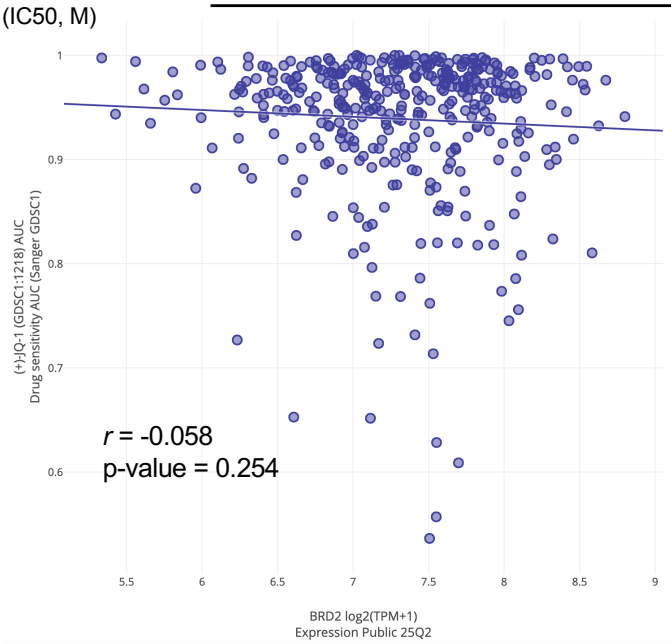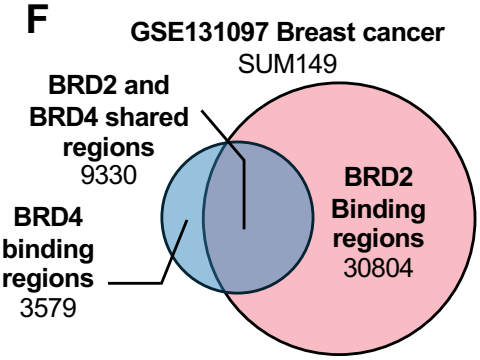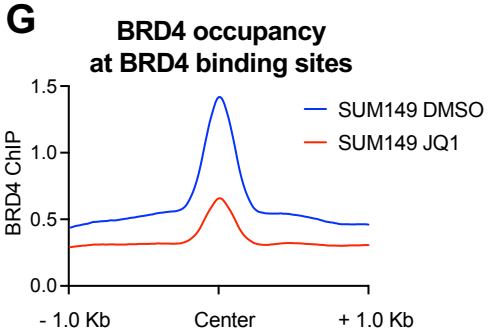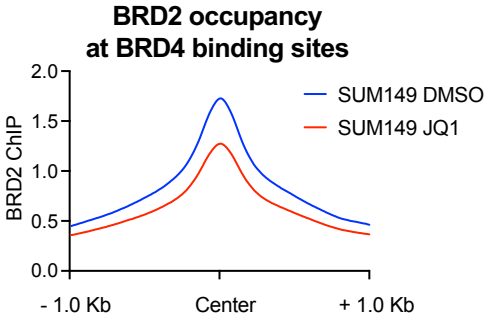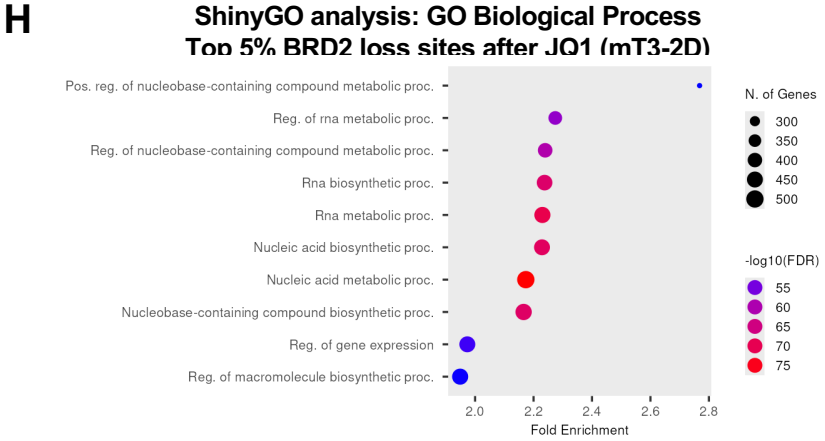
Drugs	Cell lines	LogIC$_{50}$ (M)	95% CI
JQ1	mT3-2D	-6.989	-7.139 to -6.841
	mT23-2D	-4.583	-4.775 to -4.419
Molibresib	mT3-2D	-5.875	-5.969 to -5.779
	mT23-2D	-3.605	-3.754 to -3.393
Birabresib	mT3-2D	-6.598	-6.713 to -6.479
	mT23-2D	-4.623	-4.751 to -4.496